

# Subchannel modeling of single rod bowing in a bundle geometry

Roman Mukin<sup>\*a</sup>, Riccardo Puragliesi<sup>a</sup>, Marco Pecchia<sup>a</sup>, Marcus Seidl<sup>b</sup>

<sup>a</sup>*Paul Scherrer Institute, CH-5232 Villigen PSI, Switzerland*

<sup>b</sup>*Preussen Elektra GmbH, D-30457 Hannover, Germany*

---

## Abstract

During operation of a nuclear power plant, nuclear fuel assemblies in a reactor core are in strong temperature and radiation fields. With fuel burnup and the presence of thermo-mechanical stresses, gaps between fuel assemblies start to increase, leading to permanent fuel assembly bowing. The importance of fuel assembly bowing has been emphasised in the past for various reasons, one of which is an additional correction factor in models predicting the departure from the nucleate boiling ratio (DNBR). Before modelling bowing of entire fuel assembly rod bundle, it is important to fully understand the case of single rod bow first.

In this study, an assessment of subchannel code CTF v3.5 in addressing the effect of rod bowing on DNBR is performed. Two well-known approaches for the critical heat flux (CHF) prediction are used: the W3 correlation and Groeneveld look-up table. Four different rod bowing geometries in a  $4 \times 4$  rod bundle from the CHF data bank [1, 2] are modelled: rod bowing with a gap closure of 50% and 85% of the nominal gap, and two configurations of rod bowing to contact. Comparison of calculated critical power resulted in an agreement of  $\pm 10\%$  with measured values for the straight rod bundle and partial rod bowing configurations. Results for the rod bowing to contact tests are less in agreement with the experimental values. An explanation of CHF reduction due to rod contact is suggested. It is related to the change in affected subchannel coolant flow distribution and heat transfer from the heated rods to the coolant. This conclusion is also supplemented by a detailed CFD simulation of a two-rod model. Illustrative calculation of internal rod power, obtained with neutron transport code SERPENT, has shown that rod bowing leads to internal rod power redistribution as such that it reduces high local wall temperature at the contact point.

*Keywords:* rod bowing, bowing, subchannel, COBRA-TF, CTF, DNBR, critical heat flux, CHF

---

<sup>\*</sup>Corresponding author: Roman Mukin, roman.mukin@psi.ch

## 1. Introduction

One of the most crucial limitation criteria in operation of nuclear reactors is the threshold of operating power at which fuel rods remain sufficiently cooled and with certain confidence will not be overheated. However, during the operation of a nuclear power plant, fuel assemblies (FA) may bow in the core due to non-uniformity of power distribution in the core and the thermo-mechanical loads. Such displacements from the designed geometrical parameters have a non-trivial effect on the safety analysis leading to the requirement of an in-depth analysis of the neutronic and thermal-hydraulic simulation models. In Pressurized water reactors (PWR) one of the specified safety limits is the departure from the nucleate boiling ratio (DNBR), which is the ratio of the heat flux at which the departure from nucleate boiling occurs, the so-called critical heat flux (CHF), over the actual local heat flux. DNB is a complex phenomenon; besides dependencies on the local heat transfer conditions and cladding surface and moderator material parameters, it also depends on the geometric complexity of the FA design as well as distances between them. FA internal geometrical parameters (rod pitch etc.) remain the same due to spacer grids which are holding rods in their position. During FA bowing the nominal gap between the assemblies in the core is changing from 2 mm to zero, i.e. when assemblies may touch each other, or to a much larger size around 20 mm [3]. FA bowing might cause many interconnected physical phenomena. For instance, it changes the size of flow area between rods, thus affecting the reactivity and the thermal-hydraulic parameters [4] in the vicinity of the gaps. Permanent grid-to-grid contact also changes the stresses on a FA which may lead to plastic, non-uniform deformations [5] during irradiation.

Because of the lack of experimental data on thermal-hydraulic assembly bowing analysis in open literature, application of available data on the single rod bowing is used in this work. It can be considered as the first step in the assessment and validation of subchannel code COBRA-TF (CTF) in predicting the critical power for rod bowing configurations in a rod bundle.

One of the first rod bowing experiments in PWR rod bundles published in [6]. Authors studied a diagonal rod bowing to contact with neighbour rods in PWR rod bundles. According to their conclusions, rod bowing has an effect on CHF only at high pressure ( $\sim 150 - 170$  bar) conditions. In [7, 8] rod-bundle with various rod spacings are analysed. Authors concluded that the DNBR under subcooled conditions depends primarily on the local hydrodynamics and that the CHF is reduced as the spacing of the rods decreases [7, 8]. Later, similar tests for a PWR rod bundle with  $4 \times 4$  rods for rod bowing to contact and partly rod bowing were conducted [9, 10]. Authors confirmed that a considerable effect on DNBR occurs at high pressures, whereas at low pressure ( $\sim 100 - 130$  bar) conditions the impact on DNBR is small. They observed the similar effect on DNBR for both configurations: contact to a thimble tube and contact to neighbouring rods. Influence of partial rod bowing on DNBR is only slightly greater than repeatability [10].

At the beginning of 1980's a large set of data of PWR core geometries, axial nonuniform, rod bundle CHF data points were released from the Heat Transfer Research Facility (HTRF) of Columbia University [1, 2]. Among  $\sim 11'000$  CHF data points, there are 420 data which

include tests results of different rod bowing configurations. The detailed settings of these tests are discussed in the next section.

In order to take into account the effect of rod bowing, CHF correlations can be supplemented by additional parameters. In [6] an additional correction function to W3 correlation is proposed for the case of rods in contact. This function consists of two parameters: system pressure and rod average heat flux. Since a significant effect of rod bowing on CHF was observed only at high pressure, bowing impact only applies above a certain pressure threshold that increases with decreasing system pressure. Using this assumption, authors in [9, 11] also proposed their best fitted functional form of the rod bowing effect parameter. This parameter and a relationship between bowing of the fuel rods and fuel burnup can be further processed with statistical methods to determine the margin of fuel rods DNB [4, 12].

Further experimental analysis of the rod bowing tests in a PWR tube bundle was done in [13], where authors confirmed previously obtained findings and supplemented them. For instance, they obtained that a considerable effect of rod bowing on CHF can be visible also for a gap closure of 92%; for tests with rod bowing to contact they showed a considerable effect on CHF at high subcooling, but less effect at high quality; for tests with a thimble tube the reduction of CHF is essentially similar to the same configuration with heated tubes only.

In this study, the assessment of subchannel code CTF against the CHF tests with rod bowing geometry is performed. The rod bowing CHF tests are taken from publicly available CHF data bank obtained at Heat Transfer Research Facility (HTRF) and published in [2]. For predicting DNBR two CHF models are applied: W3 CHF correlation [14, 15, 16] and Groeneveld CHF look-up table (LUT) [17]. A description of the selected rod bowing tests and subchannel representation of rod bowing geometry are presented in Sections 2 and 3. Modeling of rod bowing tests divided into three following parts in section 4. In the first part, the performance of the subchannel code CTF on the data for the reference case with straight rods is presented. The effect of flow area variation on the calculated critical power is analyzed in the section 4.2. Finally, the performance of CTF in predicting critical power for rod bowing configurations is done in the section 4.3. In addition to the subchannel analysis presented in the previous sections, illustrative calculations of two rods configuration with detailed computational fluid dynamic (CFD) and neutronic methods are presented in Sections 4.4 and 4.5.

## 2. Test description

The CHF database prepared in the mid-1980's at Heat Transfer Research Facility (HTRF) at Columbia University contains more than 11 000 data points from 235 separate test sections. Among these data, there are 420 measurements from tests number 151, 167, 168, 169 and 170 which include the effect of rod bowing.

In Figure 1 an axial part of the test section with rod bowing and the cross-section view of a tube bundle with the direction of rod bowing in the tests 167 – 170 are presented.

In this study the following five test cases were selected, see Figure 1 for the rods number:

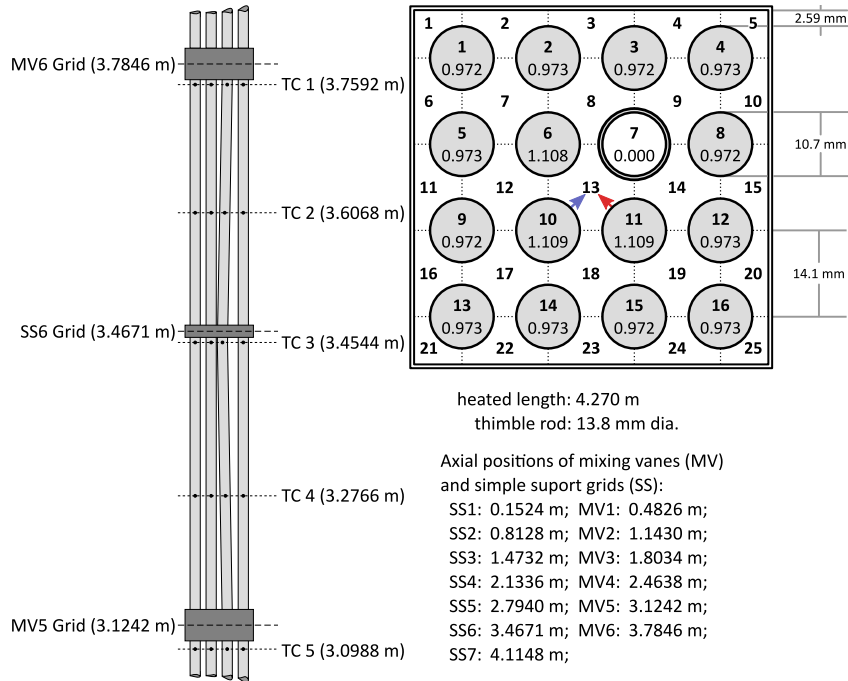


Figure 1: Axial geometry of the HTRF test section with rod bowing and cross section view of the tube bundle with the relative radial rod power distribution and subchannel numbers are given as well. Red vector is a rod displacement direction in tests HTRF 168, HTRF 169 and HTRF 170 and the blue vector is direction in test HTRF 167. MV is a mixing vane, SS is a simple support grid and TC is a thermocouple.

- HTRF 166 (no rod bowing), the reference test with a nominal configuration of rods, 47 tests;
- HTRF 167 (bowing to contact), rod 10 is bowed towards thimble tube 7 to contact rods 6 and 11, 35 tests;
- HTRF 168 (bowing to contact), heated rod 11 is bowed towards rod 6 to contact rods 7 and 10, 65 tests;
- HTRF 169 (partly rod bowing, no contact), heated rod 11 is bowed towards rod 6, reducing gap between rod 10 and thimble tube 7 to 15% of the nominal gap, 48 tests;
- HTRF 170 (partly rod bowing, no contact), heated rod 11 bowed towards rod 6, reducing gap between rod 10 and thimble tube 7 to 50% of nominal gap, 48 tests;

The tests number 151 is not selected since there is no reference test with a straight rod bundle geometry.

In all tests the point of maximum rod bowing is located at the midspan of the last two mixing vane grids. The geometry at this location was maintained by a support grid. The rod bundle has a non-uniform radial and axial power distribution, see Figures 1 and 2. All HTRF tests were conducted spanning a wide range of thermal-hydraulics (TH) parameters:

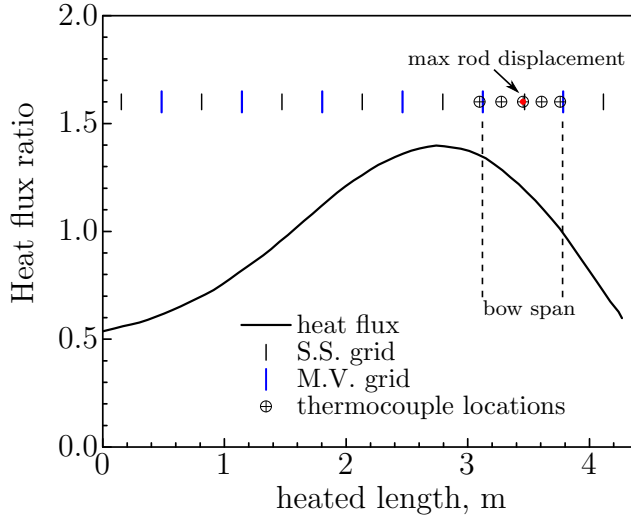


Figure 2: Axial power distribution in the selected HTRF tests.

- Pressure: 100 bar  $\sim$  160 bar
- Inlet temperature: 200 °C  $\sim$  320 °C
- Mass flow rate: 4  $\sim$  9 kg/s

The test section consists of fifteen 10.7 mm dia. rods with a heated length of 4.270 m and a 13.8 mm dia. thimble rod with a rod pitch of 14.1 mm. Two types of spacer grids were used: a mixing vane (MV) and simple support (SS) grid in between of the two MV grids. The loss coefficients are 1.25 and 0.57 for MV and SS grids respectively, taken from the HTRF tests report [2]. According to this report, in the critical power tests outlet pressure, inlet temperature, mass flow rate, axial and radial power profiles are maintained at constant conditions. The total power of a test is increased until a rod wall temperature observed signal rise by one or more thermocouples by 30°C or more. However, due to inaccuracies of the instruments and techniques for obtaining the data, there are always some uncertainties in the boundary conditions. The reported errors are quite low, the pressure uncertainty is below 0.5%, the inlet temperature uncertainty is in the range 2.2% – 2.6%, the range of mass flow rate uncertainty: 0.96% – 3.92% and measured critical power uncertainty is 0.73% – 1.10%. Despite all this relatively low uncertainty, the significant error in measuring critical power is due to thermocouples location, since wall temperature excursion may start in between the thermocouples. This uncertainty is hard to estimate. Thus it is not reported.

### 3. Rod bowing representation in subchannel code CTF

In a thermal-hydraulic analysis of rod-bundle configurations, one of the most widely used approaches is the subchannel. The main assumption in this approach is that the axial velocity component along the flow is prevailing, compared to other cross-flow components. Thereby it allows treating axial and transverse momentum equations separately. In

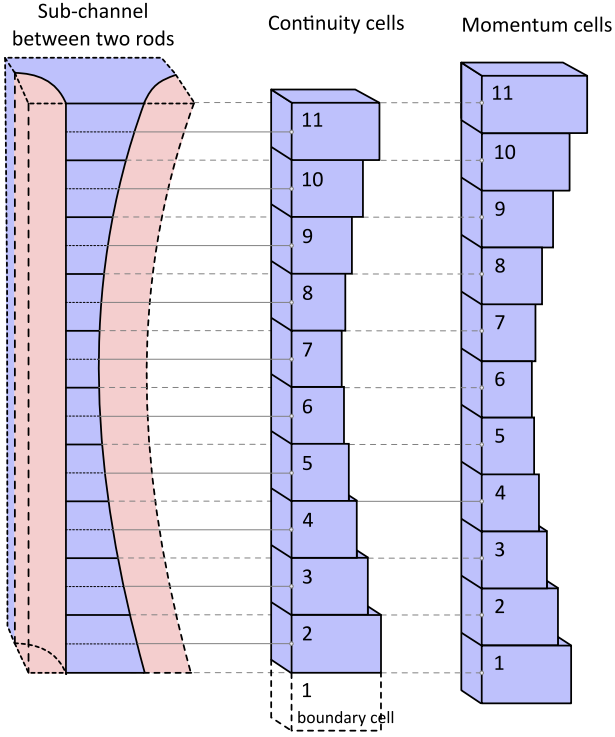


Figure 3: Example of axial flow area variation and its representation in continuity and momentum areas of a subchannel model.

transverse direction only one flow component is considered, i.e., only one flow component covers all orthogonal directions to the vertical axis. It simplifies the conservation equations dramatically from both physical and computational points of view.

COBRA-TF (CTF) is a subchannel thermal-hydraulic code used in this work. It is a two-fluid, three-field thermal-hydraulic code maintained by research groups in Oak Ridge National Laboratory and North Carolina State University [18, 19, 20, 21]. CTF solves conservation equations for the liquid, vapor and droplet phases and obtains thermal-hydraulic parameters averaged over a subchannel node. A subchannel is defined as an interconnected space between rods which is divided axially into control volumes called nodes. It is characterized by a cross-sectional area, height, and the width of the connections to the adjacent mesh cells. The conservation equations are solved using a staggered difference scheme. Continuity and energy equations are solved on subchannel centered cells, also called continuity cells. The momentum equations are solved on a staggered mesh within, the so-called momentum cells, which are centered on the continuity cell face. Within these cells, fluid properties are represented by the average values of velocity, pressure, temperature, void fraction, etc.

Figure 3 shows an example of a subchannel flow area variation between two rods if one of them is bowed. In this case, continuity and momentum cells flow area, and gaps between rods are varied. The continuity and momentum cells use the actual area at the location of the corresponding cell center.

A subchannel gap defines the control volume for the transverse momentum equation;

therefore gap variations are determined at locations of momentum cell centers. Exchange of mass, momentum, and energy in between neighboring channels occurs through the gaps between rods. In case of rod bowing to contact, the gap between rods is a number close to zero, resulting in a blockage of the lateral flow between adjacent subchannels. However, the direct heat exchange between the rods at the contact point is not considered in the subchannel method, since all heated rods exchange heat only with coolant in the subchannels. In this work code CTF version 3.5 applied across all the calculations.

## 4. Results Analysis

### 4.1. The reference test HTRF 166

We start our analysis with consideration of the reference test campaign HTRF 166 (47 tests), where all rods are straight. The boundary conditions are taken from the HTRF CHF database, the part of this database used in this work is collected in Table A.2. Screening of the tests boundary conditions revealed two inconsistencies. First, that for some cases the calculated onset of nucleate boiling is located downstream of the observed CHF location. The data point, in this case, is considered to be unreasonable. The second is that ratio between the predicted and the measured critical power is more than 1.5; this data point is also considered unreasonable and also has been filtered from the consideration. The filtering algorithm applied to the database is presented in the Appendix of this paper. The results of screening as well as the HTRF database on rod bowing is presented in Table A.2.

As it was mentioned in Section 2 the experimental procedure for obtaining the critical power is that the total power of a test is increased until a rod wall temperature observed signal rise by one or more thermocouples. In subchannel analysis, we calculate the axial distribution of DNBR values for each rod and apply a gradient descent algorithm to find total power at which DNBR is equal one for any rod and axial node. Further, in all sections, the critical power ratio parameter (calculated/measured) is used for the comparison the calculated with CTF critical power and the measured critical power.

A distinct feature of the subchannel method is that it can capture turbulent mixing and void drift in the lateral directions between adjacent subchannels. The parameter, which controls this process is called the mixing coefficient  $\beta$ , and it is defined as the ratio between transverse mass flux to axial mass flux. In CTF there are two options for this coefficient either constant or according to Rogers-Rosehart correlation [22]. This correlation depends on the ratio of hydraulic diameters of adjacent subchannels, rod diameter, and subchannel Reynolds number. Since this parameter is an unknown parameter in our subchannel model, a sensitivity for the range of  $\beta$  from 0.005 to 0.15 and Rogers-Rosehart correlation are performed. To characterize the performance of the subchannel approach following parameters are used:  $\sigma = \sqrt{\sum_{i=1}^N (P_{calc,i} - P_{meas,i})^2 / N}$  is a standard deviation of calculated critical power from the measured values and  $\mu = \sum_{i=1}^N (P_{calc,i} - P_{meas,i}) / N$  is a mean difference between calculated and measured critical power. For each step of the  $\beta$  parameter the standard deviation  $\sigma$  of the calculated critical power from the measured values is obtained, see Figure 4. As can be seen, from  $\beta = 0.10$  the standard deviation is flattened and is

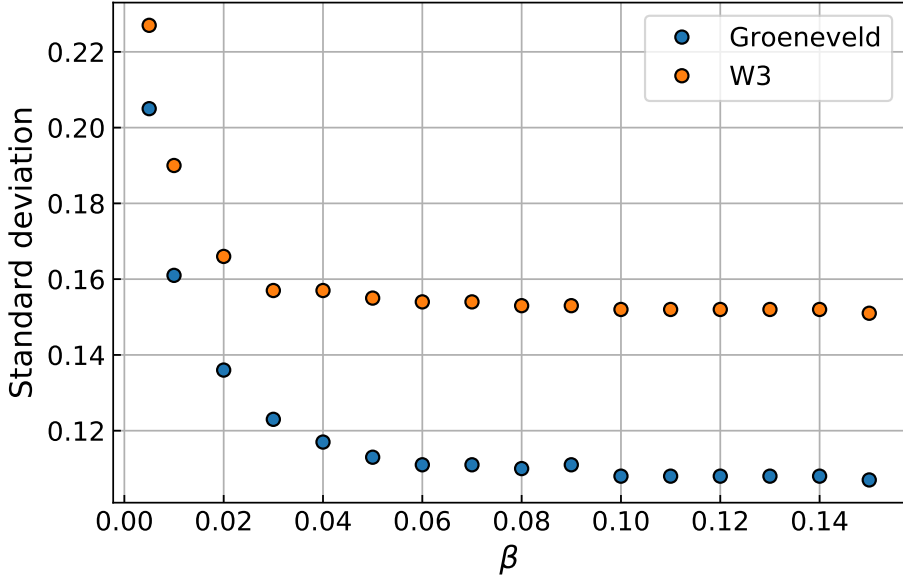


Figure 4: Standard deviation of the calculated critical power from the measured values vs the mixing factor  $\beta$  for the test HTRF 166.

independent on  $\beta$ . Thus the value of  $\beta = 0.10$  is chosen in all further analysis. Results of calculated critical power with  $\beta = 0.10$  are presented in Figure 5. For Groeneveld CHF LUT and W3  $\sigma = 0.108$ ,  $\mu = 0.085$ , and  $\sigma = 0.152$ ,  $\mu = 0.127$  respectively. The result of applying Rogers-Rosehart correlation gives  $\sigma = 0.159$ ,  $\mu = 0.138$  for Groeneveld CHF LUT, and  $\sigma = 0.187$ ,  $\mu = 0.158$  for W3 CHF correlation. As can be seen, the performance of this correlation is worse in comparison to the model with the fixed mixing coefficient. Applying Rogers-Rosehart correlation to different rod bowing configurations is not improving the performance of CTF results. Since distorted channels are only in the three axial sections nexts to the last and only four subchannels are affected by the one-rod displacement. Thus applying  $\beta$  based on the correlation can improve modeling for the distorted channels, but make much worse for all the other subchannels. Thus we decided to exclude from the further analysis consideration of the  $\beta$  coefficient correlation. Additional thoughts on our choice are written in the conclusions, Section 5.

As it was mentioned previously, there are four different rod bowing configurations. To show how rod bowing changes the critical power the same set of boundary conditions taken from the reference test and applied to the four rod bowing configurations. In the following calculations, the thermal-hydraulic boundary condition of the test HTRF 166 is used, but the geometries of the tests 167, 168, 169 and 170 applied. It indicated by ID 166-167, 166-168, 166-169 and 166-170. Thereby the immediate effect of subchannel size variations can be analyzed and compared to the reference test HTRF 166.

- HTRF 166 (no rod bowing), the reference test with a nominal configuration of rods;
- HTRF 166-167 (bowing to contact), rod 10 is bowed towards thimble tube 7 to con-

Table 1: Comparison of the subchannels flow area ratio which are affected by the rod bowing and statistical parameters of the critical power ratio distributions for different rod bowing configurations, where  $\mu = \sum_{i=1}^N (P_{calc,i} - P_{meas,i})/N$  is the average critical power ratio;  $\mu_{166-i}/\mu_{166}$  is the mean critical power ratios of cases from HTRF 166 to HTRF 166-170 and the reference case HTRF 166; MED is the median of the power ratio  $P_{calc,i}/P_{meas,i}$ ;  $MED_{166-i}/MED_{166}$  the median critical power ratios of cases from HTRF 166 to HTRF 166-170 and the reference case HTRF 166; stdv is the standard deviation of the power ratio  $P_{calc,i}/P_{meas,i}$  distributions from its average value; MAD is the median absolute deviation of the critical power ratio. 15% and 50% are the percentages of the nominal gap between rods in cases 166-169 and 166-170 respectively.

	HTRF 166 reference	HTRF 166-167 contact	HTRF 166-168 contact	HTRF 166-169 15%	HTRF 166-170 50%
	Ratio of subchannels flow area to the reference :				
subchannel number	19 or 17*: 19: 13:	<b>1.00000</b> <b>1.00000</b>	<b>1.52321</b> <b>0.39383</b>	<b>1.37388</b> <b>0.56678</b>	<b>1.30869</b> <b>0.64205</b>
	Statistical parameters of the critical power ratio ( $P_{calc}/P_{meas}$ ) distribution:				
$\mu$	W3: Groeneveld:	0.99519 0.98631	0.92805 0.95013	0.95383 0.96672	0.96468 0.97238
$\mu_{166-i}/\mu_{166}$	W3: Groeneveld:	<b>1.00000</b> <b>1.00000</b>	<b>0.93253</b> <b>0.96332</b>	<b>0.95843</b> <b>0.98014</b>	<b>0.96934</b> <b>0.98588</b>
stdv	W3: Groeneveld:	0.04765 0.03241	0.04113 0.03727	0.04187 0.03146	0.04241 0.02930
MED	W3: Groeneveld:	0.98929 0.98572	0.92630 0.94422	0.94988 0.96199	0.95940 0.97066
$MED_{166-i}/MED_{166}$	W3: Groeneveld:	<b>1.00000</b> <b>1.00000</b>	<b>0.93633</b> <b>0.95791</b>	<b>0.96016</b> <b>0.97593</b>	<b>0.96979</b> <b>0.98473</b>
MAD	W3: Groeneveld:	0.05904 0.02235	0.05004 0.03951	0.05317 0.02922	0.05440 0.02748

\* for the test HTRF 166-167.

tact rods 6 and 11, boundary conditions from the test HTRF 166, comparison with measured critical power in the test HTRF 166;

- HTRF 166-168 (bowing to contact), heated rod 11 is bowed towards rod 6 to contact rods 7 and 10, boundary conditions from the test HTRF 166, comparison with measured critical power in the test HTRF 166;
- HTRF 166-169 (partly rod bowing, no contact), heated rod 11 is bowed towards rod 6, reducing gap between rod 10 and thimble tube 7 to 15% of the nominal gap, boundary conditions from the test HTRF 166, comparison with measured critical power in the test HTRF 166;
- HTRF 166-170 (partly rod bowing, no contact), heated rod 11 bowed towards rod 6,

reducing gap between rod 10 and thimble tube 7 to 50% of nominal gap, boundary conditions from the test HTRF 166, comparison with measured critical power in the test HTRF 166;

The results for the partly rod bowing configurations with 50%, 15% of the nominal gap and two configurations of rod bowing to a contact are presented respectively in Figures 6, 7, 8, 9. As can be seen, the subchannel method is reducing critical power due to decreasing of the flow rate in the affected subchannel. More detailed analysis of how subchannels are affected by CHF is presented in the next section 4.2.

In Figure 6, results for the rod bowing with 50% of the nominal gap configuration are presented. For all selected configurations the calculated critical power is slightly reduced in comparison to the reference case. Following results for Groeneveld CHF LUT and W3 CHF correlation are obtained:  $\sigma = 0.110$ ,  $\mu = 0.091$ , and  $\sigma = 0.143$   $\mu = 0.121$  respectively. Almost no change in case of Groeneveld CHF LUT and around 4% to 5% change of  $\sigma$  and  $\mu$  for W3 CHF correlation can be explained by the higher dependence of W3 CHF correlation on the mass flux than in the Groeneveld CHF LUT. In the next rod bowing configuration the gap between displaced rod and the thimble tube is reduced to 15% of its nominal value. The calculated critical power is reduced more compared to the previous case, see Figure 7. This can also be seen in the increased values of standard deviation  $\sigma$  and the mean difference between the calculated and the measured values.

Rod bowing configurations with contact to neighbor rods lead to a more substantial decrease of the critical power than in the previous cases with partly rod bowing, see Figures 8 and 9. Since in the rod bowing to contact cases, the affected subchannels flow area is reduced more than in the previous cases, thus the reduction of the calculated critical power is more significant. In Table 1, the maximum flow area ratios to the reference case and critical power ratios for the affected subchannel with minimum flow area, where the mass flow rate of coolant is reduced, are presented. It allows to see how the reduced flow area changes the critical power ratio. In case of rod bowing to contact HTRF 166-167 the maximum reduction of the flow area occurs in subchannel 13 (around 60%, see Table 1), thus it reduces the mass flow rate of the coolant in this subchannel, and consequently the maximum reduction of the critical power is observed for this case. In the case of HTRF 166-170, the reduction of the flow area is around 20% with almost no effect on the critical power. Another outcome from the comparison of the CHF models performance in Table 1 is that the difference between the CHF models is not significant. W3 CHF correlation predicts a larger reduction of the average critical power ratio with  $\sim 7\%$ , on the contrary to the Groeneveld CHF LUT with  $\sim 4\%$ . As it was mentioned in the Section 3, the subchannel approach does not take into account the direct heat transfer between rods in contact, i.e., rods are releasing heat only to respective subchannels which are attached to them.

For the graphical representation of all results in this section and comparison of the critical power ratio distributions for all tests a boxplot method is applied. The boxplot is a very well known method in a descriptive statistics; it allows to make a graphical representation of data sets distributions to show the spread and skewness between different groups of data. In Figure 10 such boxplots are presented for the critical power ratio distributions of HTRF

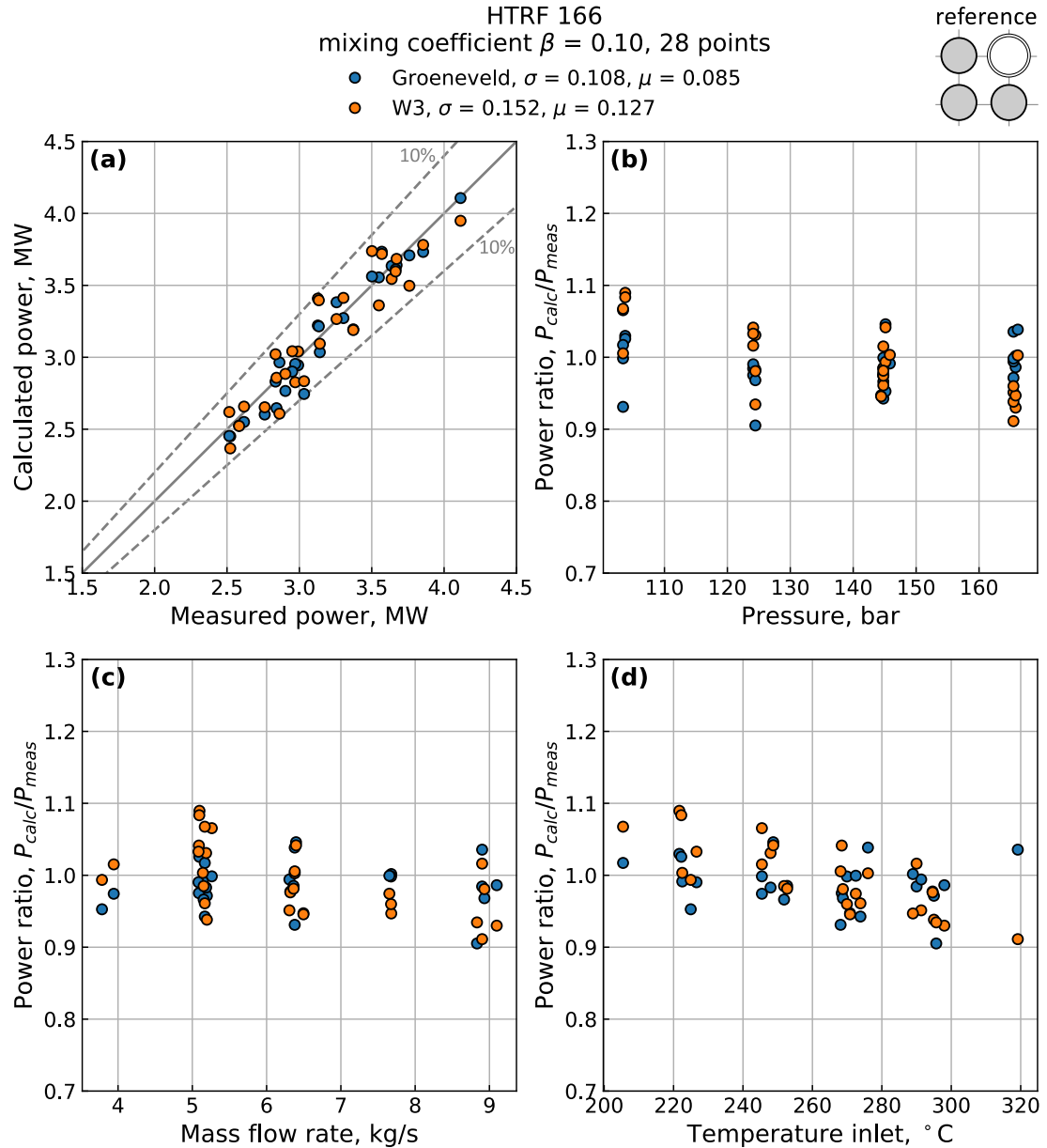


Figure 5: Comparison of calculated critical power to the measured values for the test HTRF 166 (the reference case with no rod bowing configuration) with the selected 28 points and mixing coefficient  $\beta = 0.10$ , where  $\sigma$  is the standard deviation of the calculated critical power from the measured value,  $\mu$  is the mean difference between the calculated and measured critical power, the power ratio is the ratio between the calculated with CTF critical power and the measured value in the reference test HTRF 166.

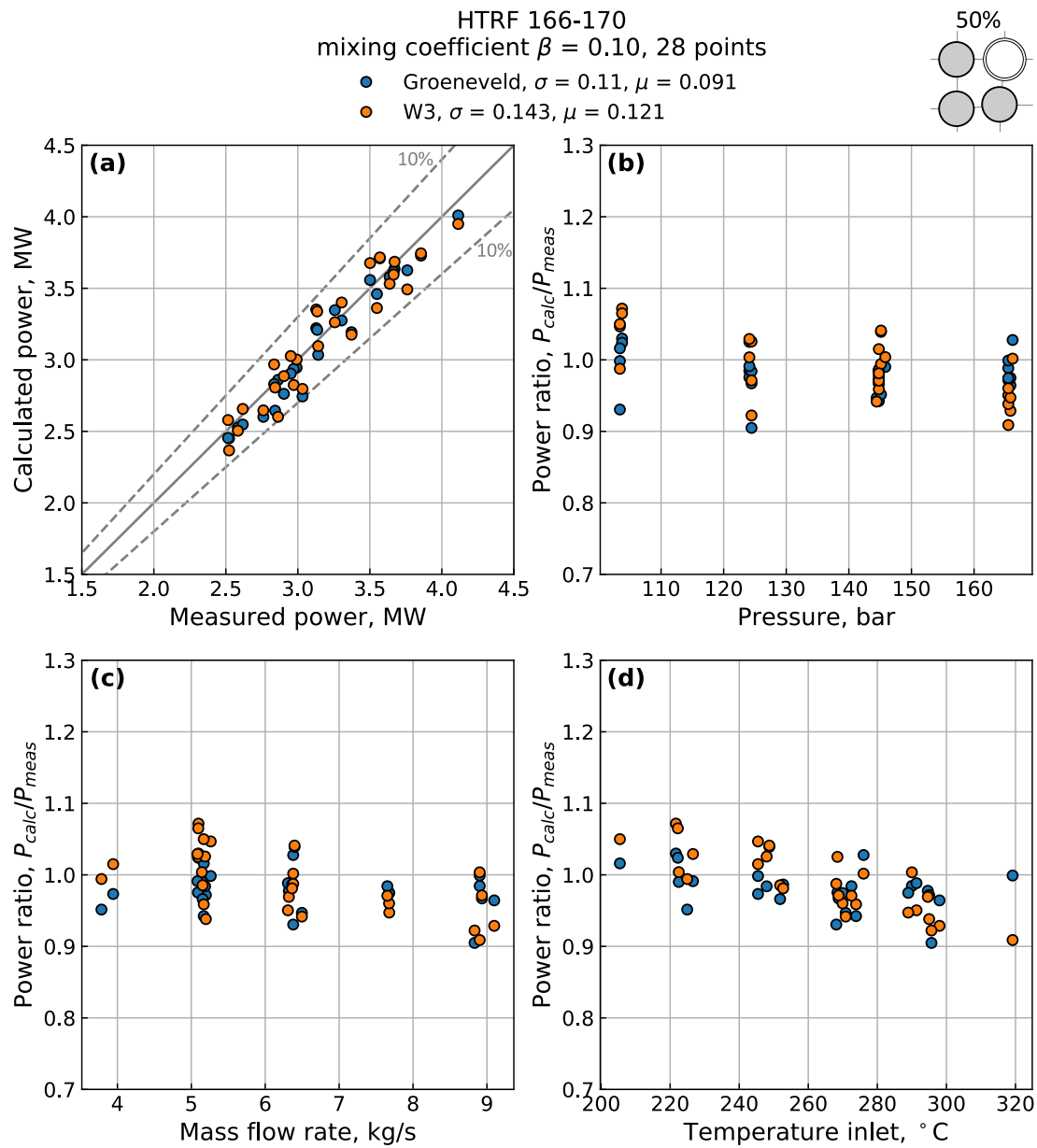


Figure 6: The same as in Figure 5, but rod bowing configuration as in the test HTRF 170 (with no contact to the neighbour rods), and with boundary conditions for the reference test HTRF 166 and comparison with measured critical power  $P_{\text{meas}}$  in the test HTRF 166.

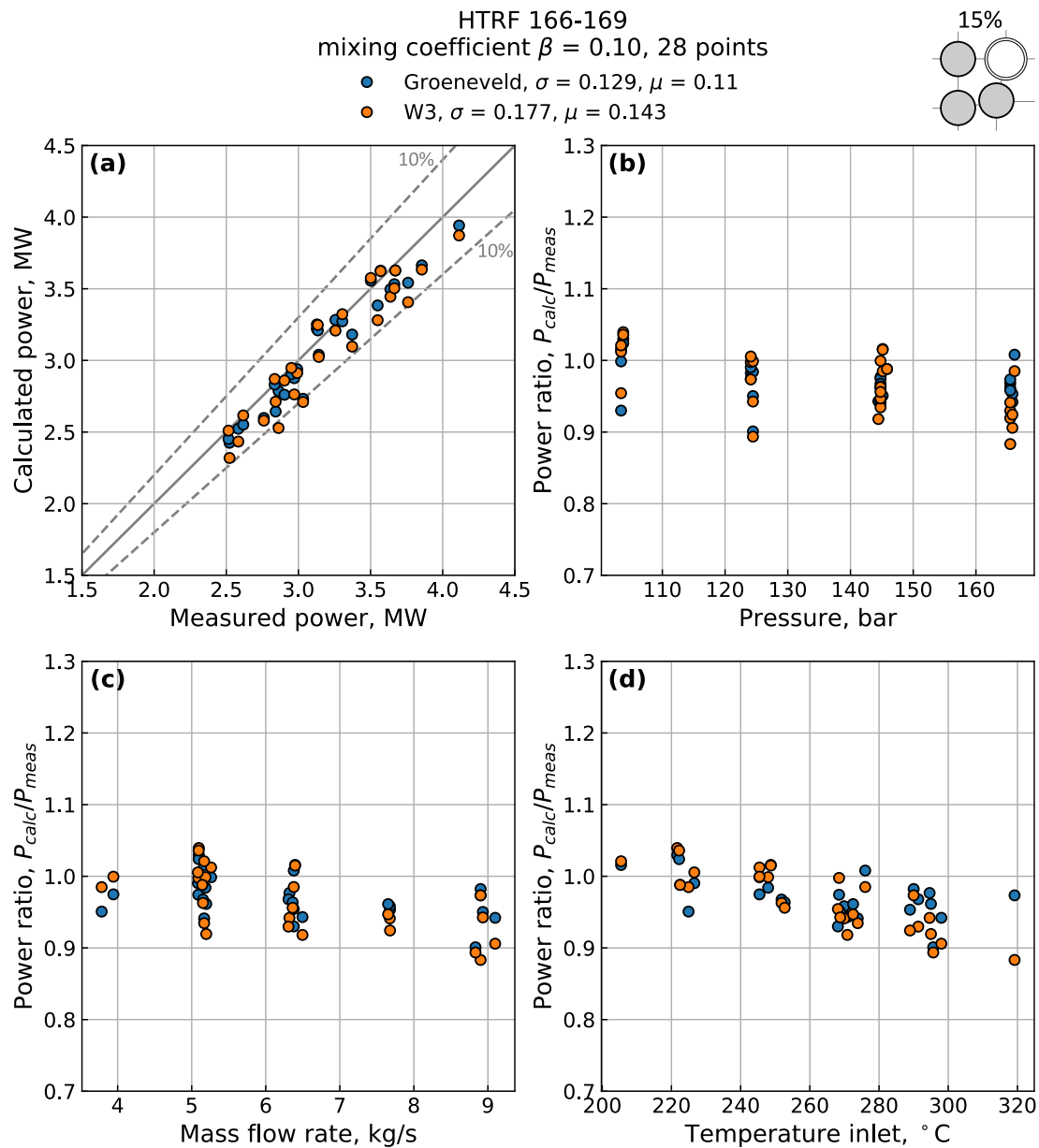


Figure 7: The same as in Figure 5, but rod bowing configuration as in the test HTRF 169 (with no contact to the neighbour rods), and with boundary conditions for the reference test HTRF 166 and comparison with measured critical power  $P_{\text{meas}}$  in the test HTRF 166.

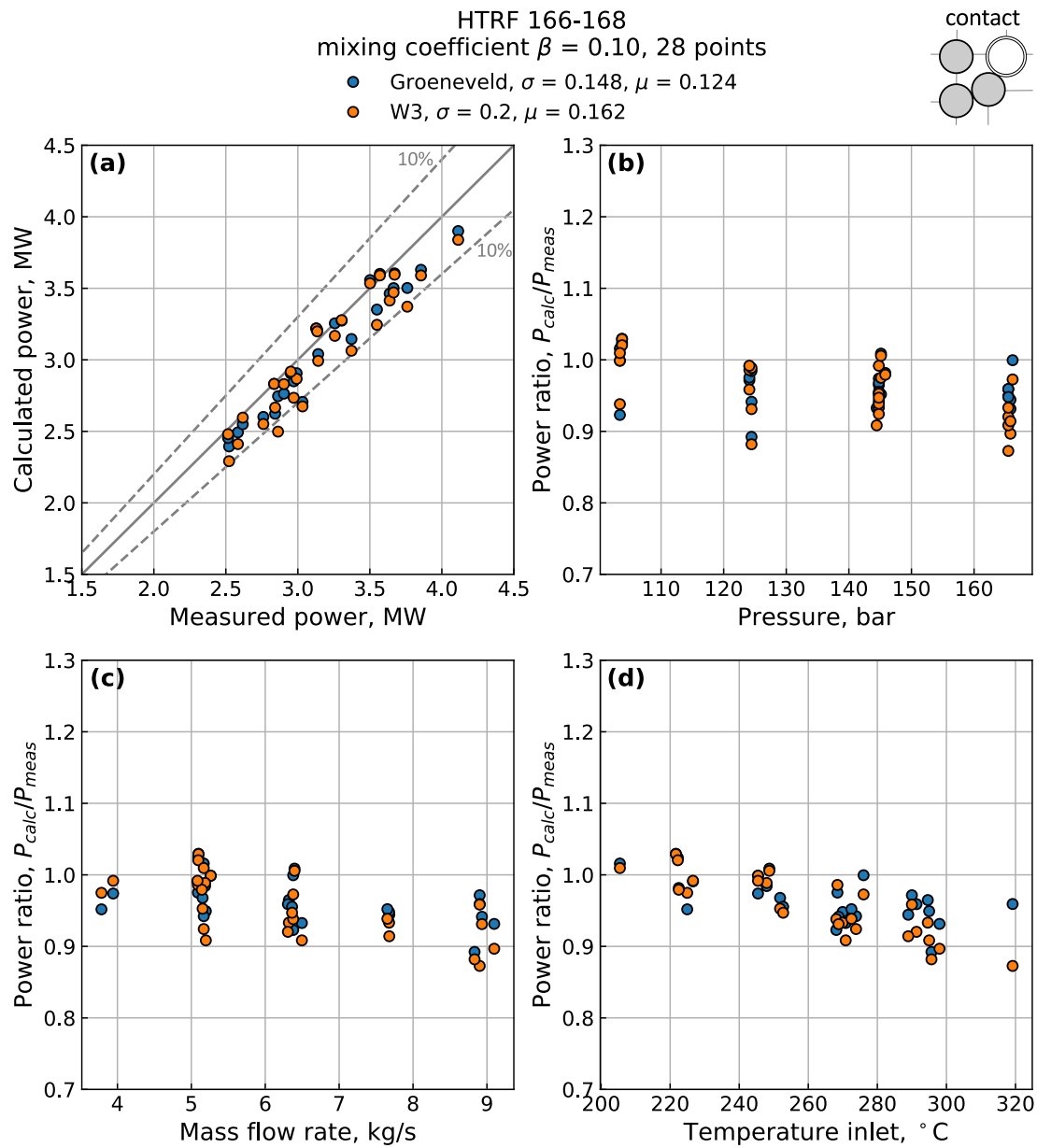


Figure 8: The same as in Figure 5, but rod bowing configuration as in the test HTRF 168 (with contact to the thimble rod), and with boundary conditions for the reference test HTRF 166 and comparison with measured critical power  $P_{meas}$  in the test HTRF 168.

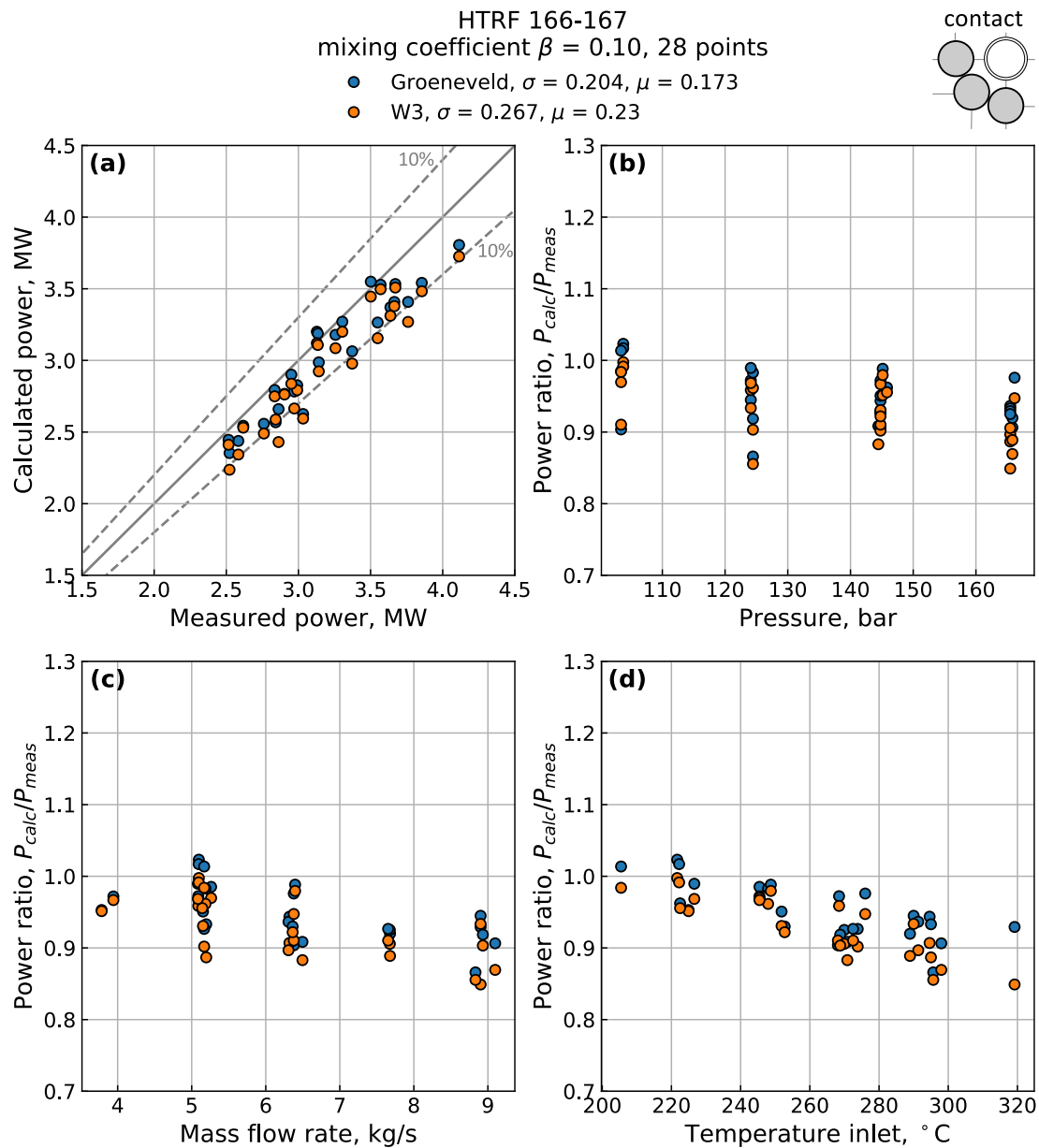


Figure 9: The same as in Figure 5, but rod bowing configuration as in the test HTRF 167 (with contact to the neighbour rods), and with boundary conditions for the reference test HTRF 166 and comparison with measured critical power  $P_{\text{meas}}$  in the test HTRF 166.

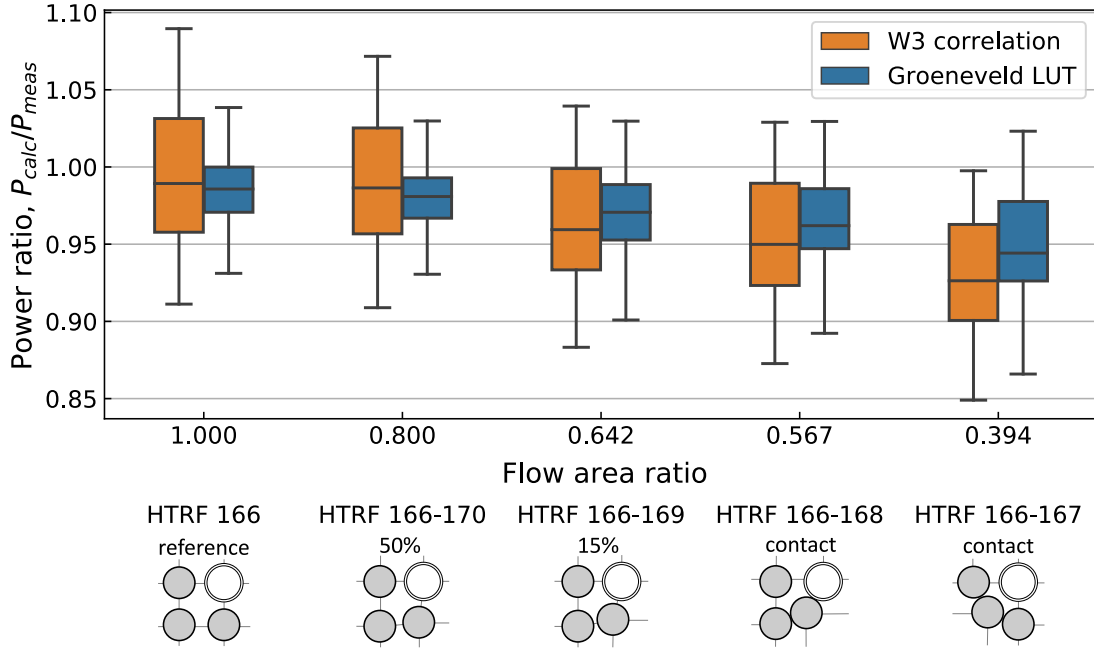


Figure 10: Boxplot representation of the critical power ratio  $P_{\text{calc}}/P_{\text{meas}}$  distributions, where  $P_{\text{meas}}$  is the measured value of the critical power for the reference test HTRF 166.

tests considered in this section. The bottom and the top of the colored boxes, in this figure, represent the first and third quartiles, and the line inside the box is the median for the respective data sets of the critical power ratio. The lines extending parallel from the boxes are known as the "whiskers", which are used to indicate variability outside the upper and lower quartiles. Figure 10 shows that the prediction for the case with two rods in contact lies outside the fourth quartile and hence justifies a review of the subchannel model suitability for this case. The spread of the power ratios obtained for the reference test HTRF 166 remained the same for the partly rod bowing with 50% from the nominal gap, but it is getting more wide with increasing the rod bowing or reducing the flow area. The reason for this is that at high values of the mass flux, pressure or temperature, the CHF is stronger dependent on the mass flux variation than at lower ones. From Figure 10, it is also clear that W3 CHF correlation gives the more substantial reduction of the power ratio compare to Groeneveld CHF LUT. Overall conclusion for this section is that subchannel method qualitatively captures an effect caused by rod bowing on the critical power via changing the flow area and gaps sizes of the affected subchannels. The quantitative assessment is given in Section 4.3.

#### 4.2. Effect of flow area variation on CHF

In this section results of subchannel calculations for two individual subchannels 13 and 19, which are affected the most by rod bowing are presented for the test HTRF 166-169, see Table A.2 for the boundary conditions. Two different kinds of CHF approaches are employed in this work. First, W3 CHF correlation is widely used for PWR type of assemblies [16]. It

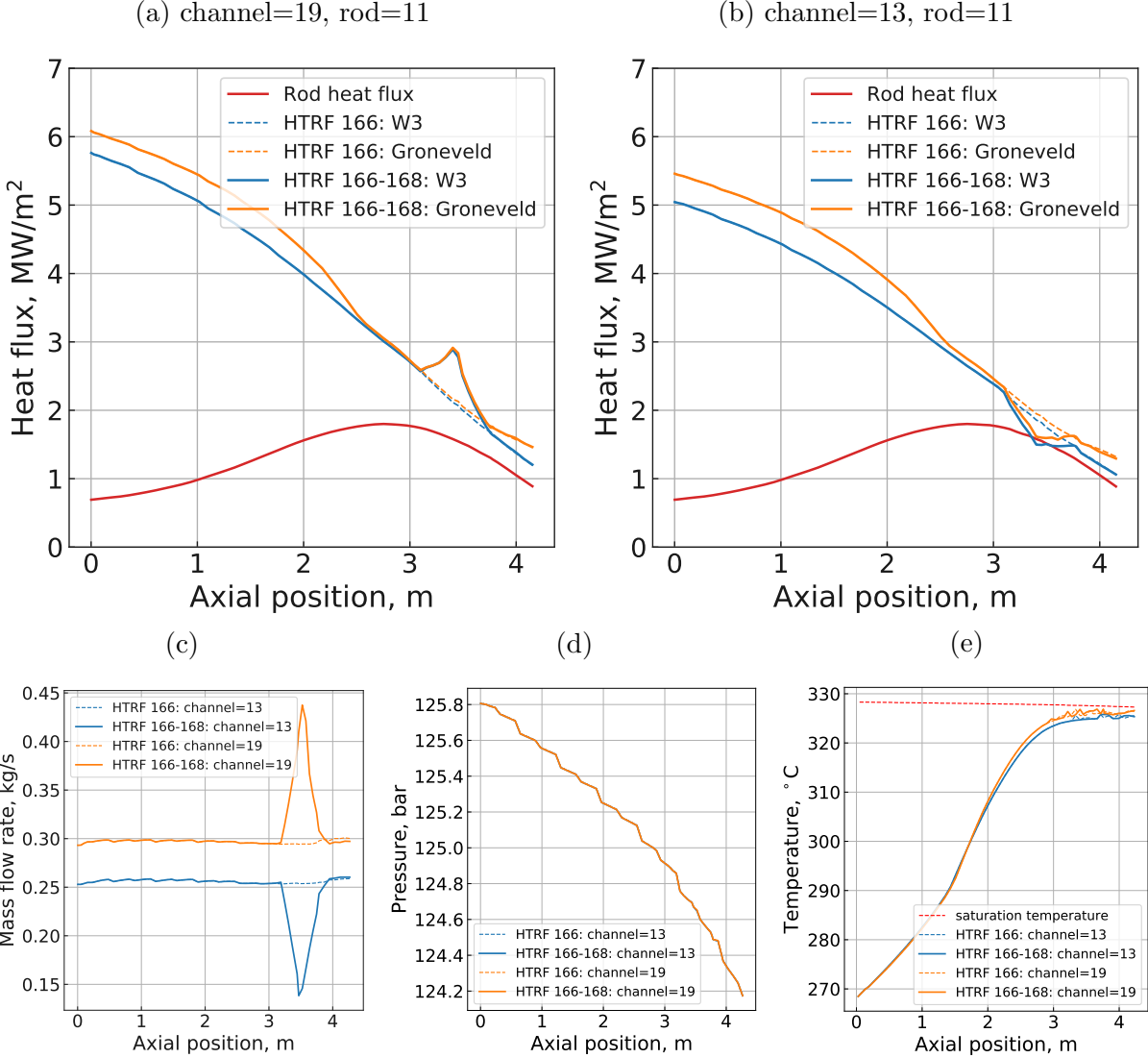


Figure 11: CHF comparison between the reference test HTRF 166 and test HTRF 166-168 with rod bowing to contact for two subchannels 13 and 19. (c), (d) and (e) are the axial mass flow rates, pressure and temperature distributions for the selected subchannels.

is based on empirically correlated independent functions of flow quality vs. pressure, mass flux, wetted perimeter and inlet enthalpy. This correlation also includes a dimensionless grid (or spacer) factor and a shape factor (or Tong factor), which takes into account the grid effect and heat flux non-uniformity respectively. Second, Groeneveld CHF LUT is a tabulated form of measured CHF (approx. 26000 data points) at a vast range of main thermal-hydraulic parameters (pressure, temperature, mass flux, and flow quality) in tests with a single tube [17]. To take into account tubes with different hydraulic diameters  $D_{hyd}$ ,

CHF LUT has a simple empirical correction factor  $K_1$  in the following form:

$$K_1 = \begin{cases} 1.633, & D_{hyd} < 3 \text{ mm} \\ (0.008/D_{hyd})^{1/2}, & 3 \text{ mm} \leq D_{hyd} \leq 25 \text{ mm} \\ 0.57, & D_{hyd} > 25 \text{ mm} \end{cases}$$

In addition to  $K_1$  in the subchannel code CTF there is also implemented a heated length correction factor  $K_4$ . Descriptions of all correction factors proposed by Groeneveld can be found in [17].

W3 CHF correlation takes into account the variation of the flow area implicitly via changes of the mass flux, while Groeneveld CHF LUT includes also the correction factor  $K_1$ . To compare how these CHF models react to the change of a subchannel flow area, two subchannels 13 and 19 with the maximum flow area variations are selected, see Figure 1. In Figure 11 the result of CHF comparison between Groeneveld CHF LUT and W3 CHF correlation is presented. As can be seen, both models show the increase of CHF due to the flow rate increase as a consequence of the larger flow area. For the subchannel with the reduced flow area, the CHF is decreased in both CHF models. Quantitative comparisons of how CHFs are changing along the selected subchannels are presented in Figure 11a. Both CHF models show the similar response to the variation of the flow area. As can be seen in Figures 11c, 11d and 11e main contribution to the variation of CHF is given by the change of the local mass flow rate.

#### 4.3. HTRF tests with bowed rod

After presenting how subchannel code CTF takes into account rod bowing, the quantitative comparison of all tests with rod bowing (from HTRF 167 to HTRF 170) is performed. The comparison results of the calculated critical power to the measured values are presented in Figures 12, 13, 14 and 15. All figures show the larger standard deviation of calculated critical power from the measured values in comparison to the reference test HTRF 166.

In Figures 12 and 13 the critical power ratio ( $P_{calc}/P_{meas}$ ) for two tests HTRF 167 and HTRF 168 with rod bowing to contact are presented.

Results of the partially rod bowing tests HTRF 169 and HTRF 170 are presented in Figures 14 and 15. The spread of power ratio results is not that large as in the previous rod bowing tests to contact, and it is comparable to the reference test, see the values for the standard deviations. As can be seen, the trends obtained previously for the reference case are also captured here. For high mass flow rates and high inlet temperatures, the calculated critical power is underpredicted, at high pressures there are only a few points thus it is very hard to conclude about any trends there.

Comparison of power ratio distributions for all HTRF tests is presented in Figure 16. It shows that the rod bowing to contact has a significant effect on the critical power ratio distribution. From the vast spread of the critical power distribution for both rod bowing to contact tests, the deteriorated performance of the subchannel method in predicting the critical power can be concluded. As it was mentioned before, the subchannel approach does not take into account the actual contact of the rods. It also explains rather good agreement

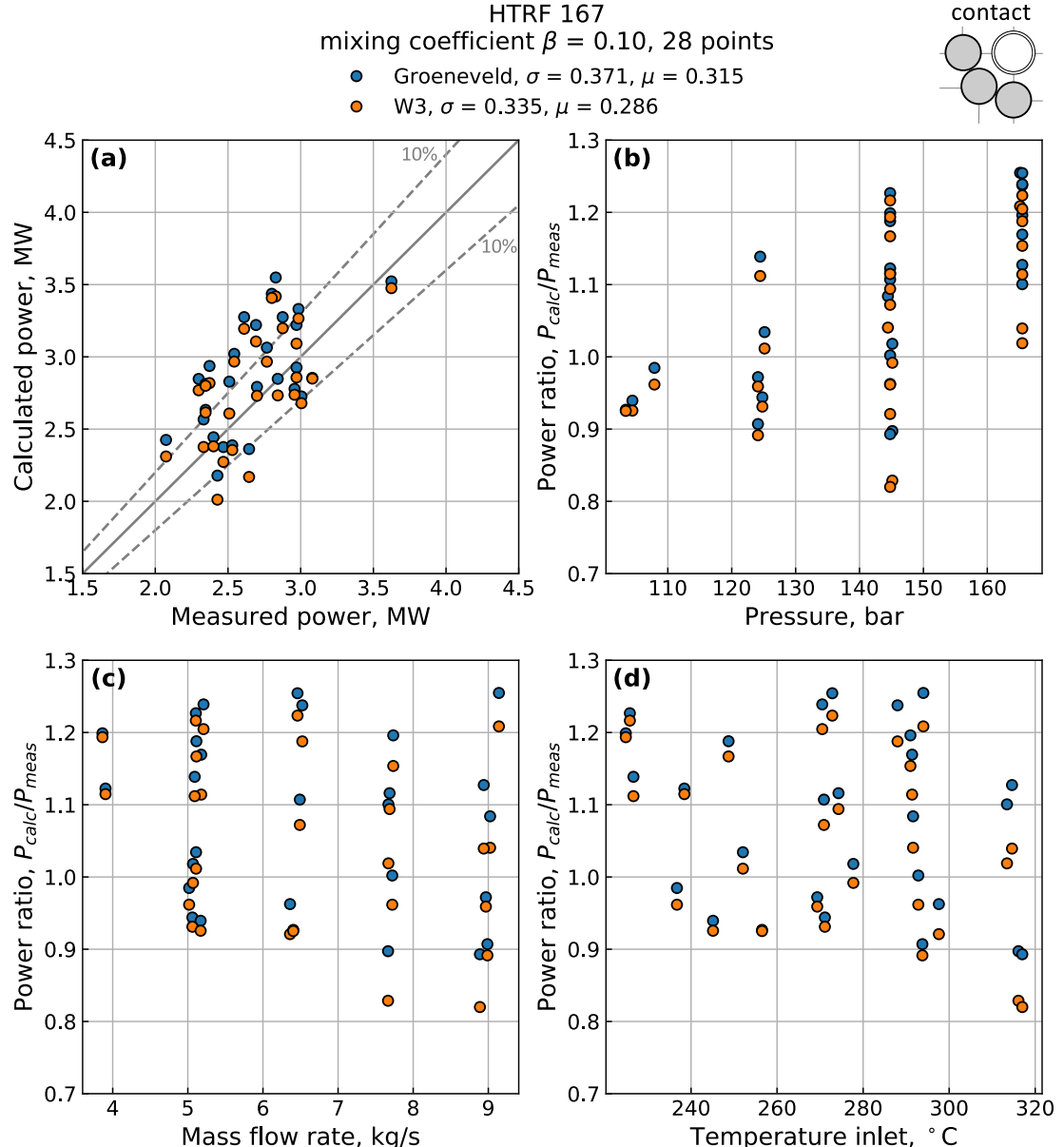


Figure 12: Comparison of calculated critical power to the measured values for the test HTRF 167 (the rod bowed configuration with contact with neighbour rods) with the selected 28 points and mixing coefficient  $\beta = 0.10$ , where  $\sigma$  is the standard deviation of the calculated critical power from the measured value,  $\mu$  is the mean difference between the calculated and measured critical power and power ratio is the ratio between calculated critical power and measured value.

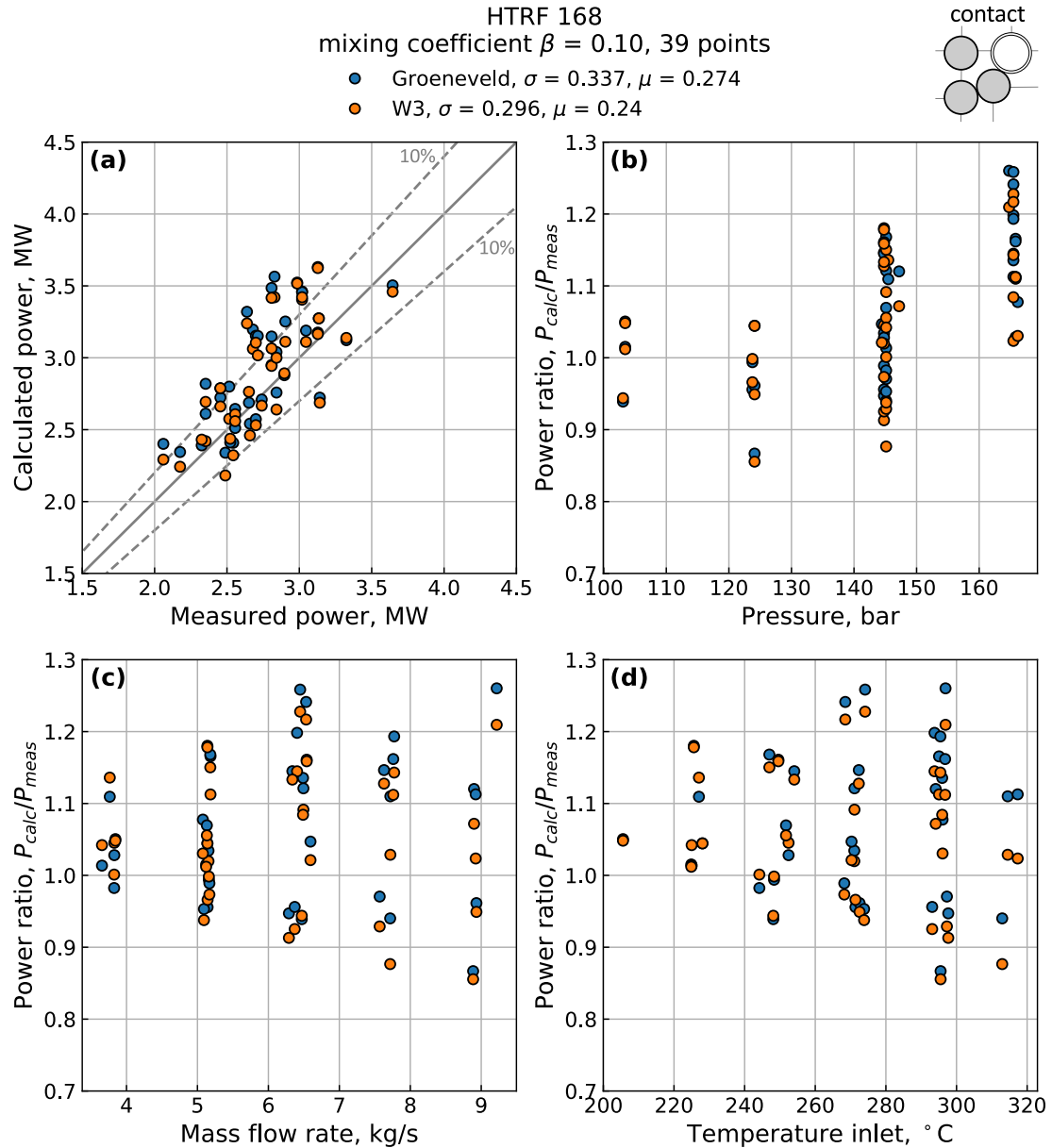


Figure 13: Same caption as in Figure 12, but comparison is done for the test HTRF 168 (contact to the thimble rod).

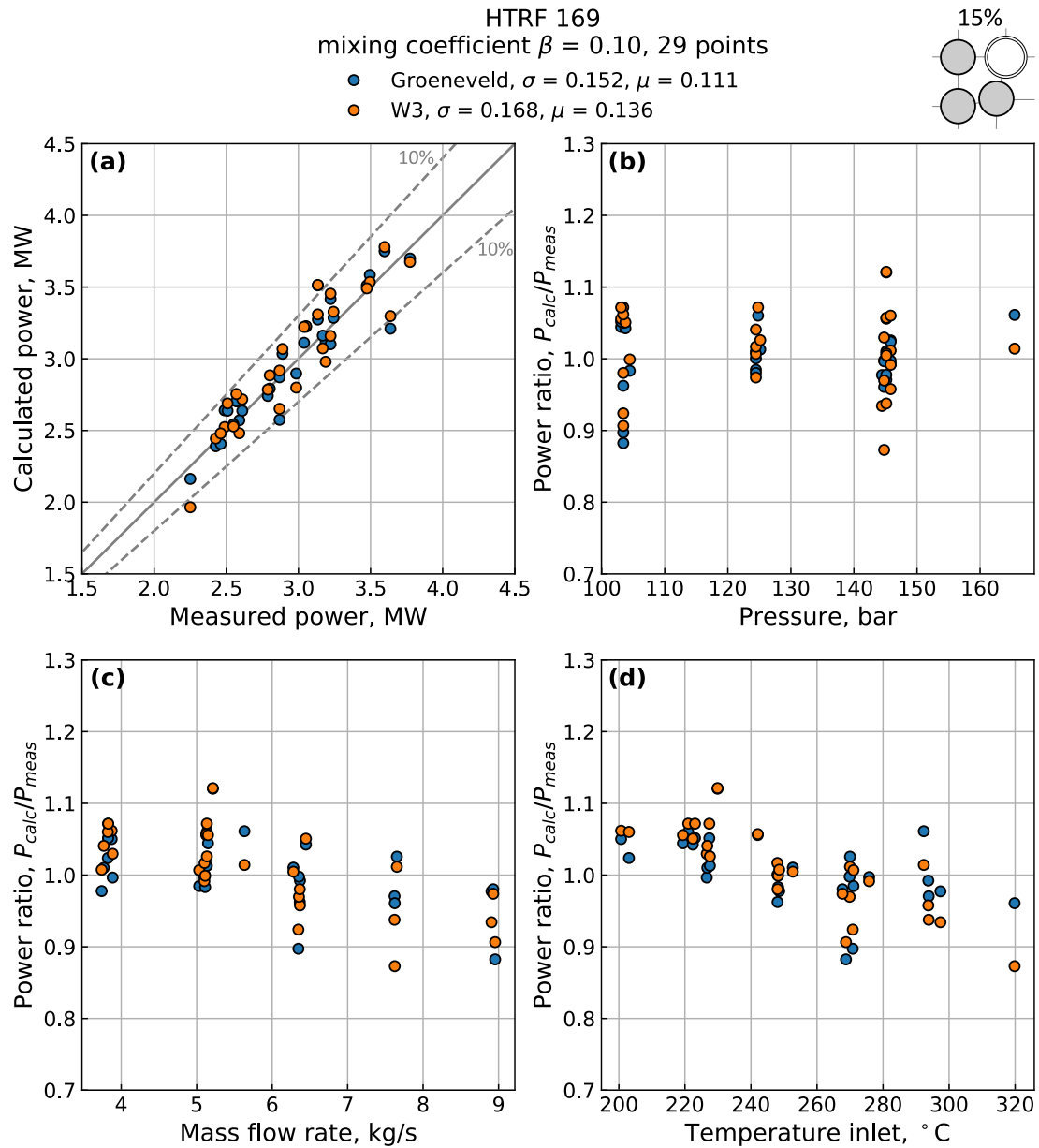


Figure 14: Same caption as in Figure 12, but comparison is done for the test HTRF 169 (partly rod bowing test with 50% of the nominal gap).

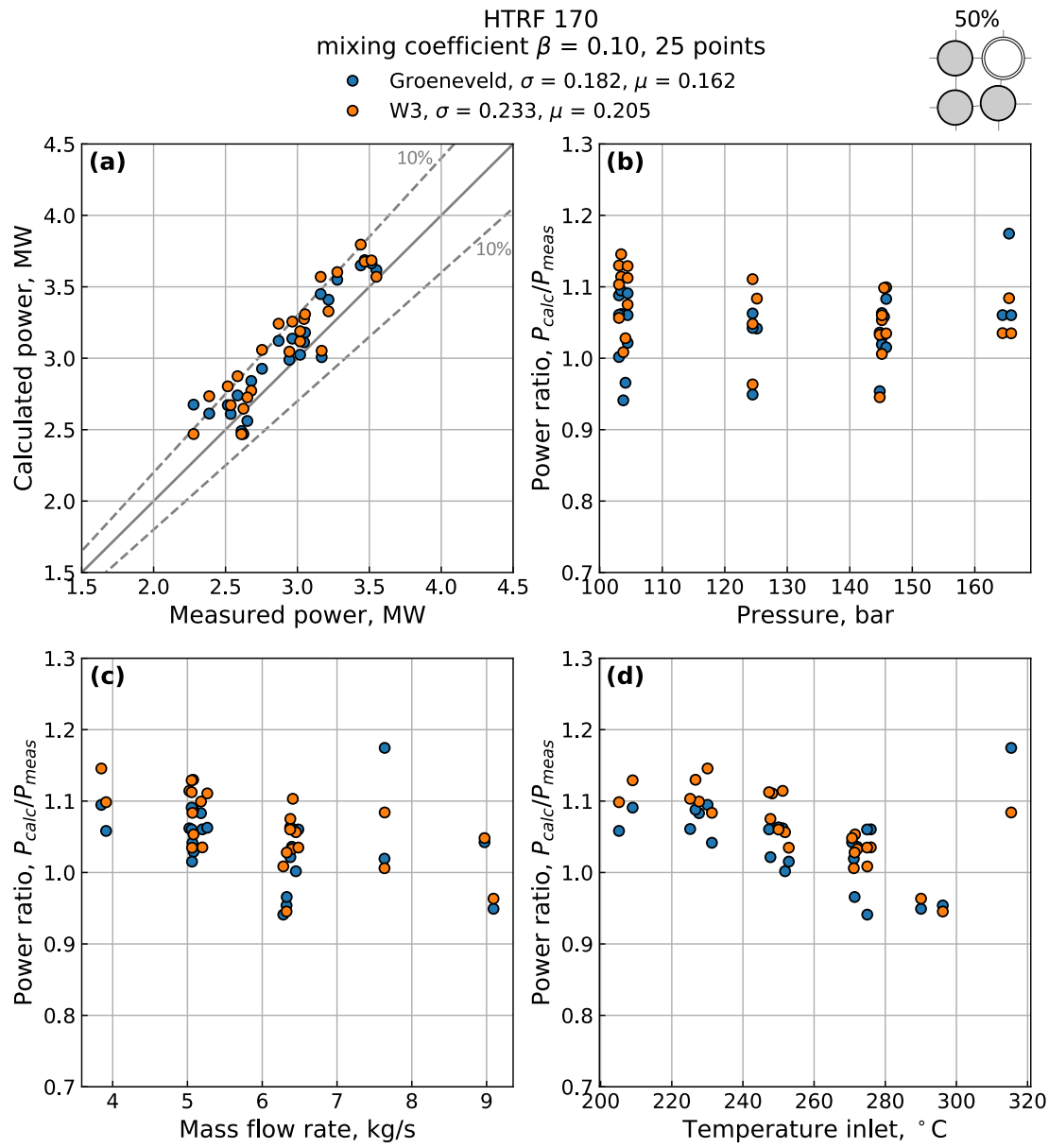


Figure 15: Same caption as in Figure 12, but comparison is done for the test HTRF 170 (partly rod bowing test with 85% of the nominal gap).

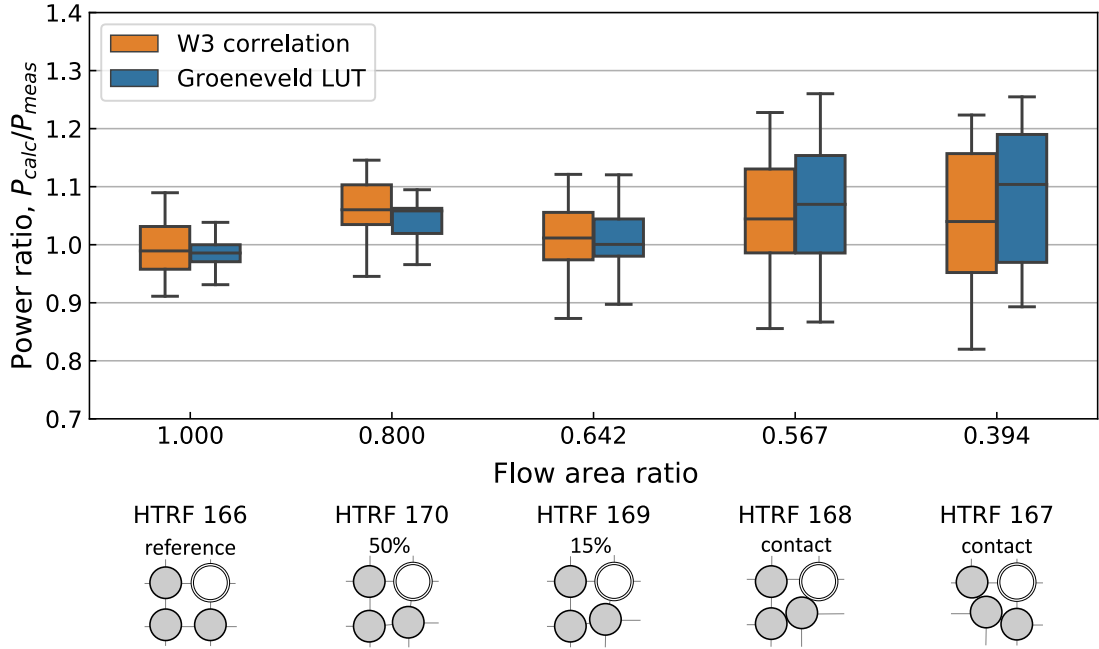


Figure 16: Boxplot representation of the critical power ratio distributions for each HTRF tests.

for the partly rod bowing tests. Since in this case variations of the flow area are not affecting the critical power significantly, see also results for the HTRF 166-169 and 166-170.

Overall, the subchannel method for both CHF models in all rod bowing tests tends to over-predict the critical power (less conservative). The widespread of the critical power ratio distributions in the tests HTRF 167 and 168, can be explained by the fact that the point of contact between two rods is not modeled in the subchannel method. The effect of the rod bowing in the subchannel method is taken into account only by modifying rods gap size and subchannels flow area. However, as it will be shown with the CFD method in the next Section 4.4 the rods contact point is changing quite dramatically the heat transfer at the contact area.

#### 4.4. A two-rod CFD model

It is well known that subchannel codes provide thermal-hydraulic solutions of the core at a rather coarse level when compared to CFD solutions. This approach is acceptable for a large variety of phenomena for which the average flow field and regime govern the physics of such a large system because of the very high computational resources required for CFD. In the present case, a localized perturbation of the geometry is introduced in the system by imposing a deformation of a single central rod in the entire assembly which directly affects the flow area and the flow distribution around the heated rod. The imposed rod deformation is of P-type, whereas the thimble is kept undeformed (see Figure 17). Using a low-resolution model, that is not equipped with ad-hoc correlations created to better approximate phenomena induced by localized perturbation, might result in a solution where

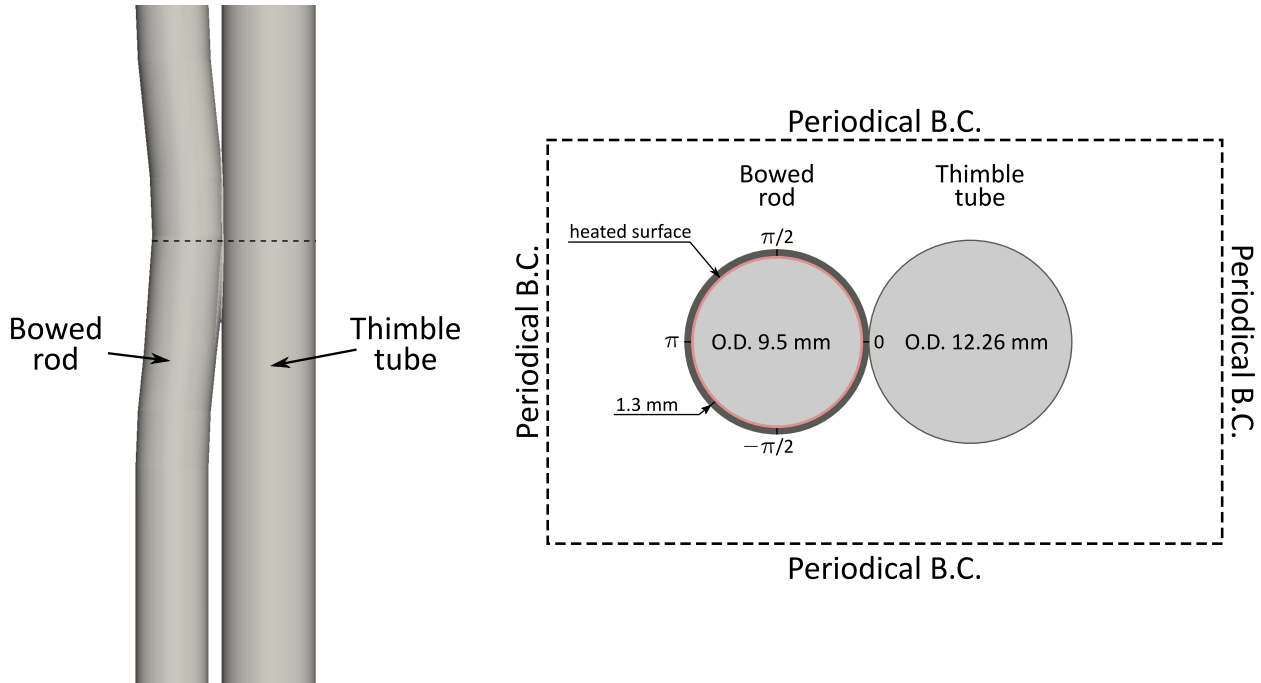


Figure 17: Schematic representation of the P-shape rod deformation with solid structures in contact. On a left is the side view and on the right is a top view at the contact point.

the effect caused by the local disturbance can be much smaller in its intensity than in the actual system. Eventually, this might induce a misjudgment of the importance of such local effect. This is one of the main reasons why high-resolution methods exist and are needed for studying and understanding systems with relevant physical phenomena that are local.

In this section, a simplified CFD model created in STAR-CCM+ v.11.6 is used to illustrate how local quantities at the surface of the heated rod are affected by the local rod deformation. Because the model is simplified/idealized as in [23], the results shown here serve only for illustrative purposes. Indeed the present CFD physical model does not resolve the phase change at the wall where subcooled boiling is expected and no grids are inserted in the computational domain. These two essential details will be factored in future work. The rod and the thimble tube diameters are taken from [24] (external rod diameter is 9.5E-03 m, the inner diameter is 8.2E-03 m and the thimble outer diameter is 12.26E-03 m) and the inter-axial distance is fixed to 12.6E-03 m for the nominal, i.e. non-deformed, configuration. The full heated length is modeled (i.e. 3.658 m). The material properties of the rod correspond to those of INCONEL 600 [24] and are function of the solid temperature while the liquid properties are considered everywhere uniform at the system conditions of ( $P = 15.6$  MPa,  $T = 530.0$  K). The coolant flow is also supposed to be incompressible, Newtonian and turbulent. The foreseen solution is steady-state and for such reason the Reynolds averaged Navier-Stokes equations are solved together with the two-equation  $k - \epsilon$  turbulence model where a low  $y_+$  wall treatment is chosen. The latter choice is justified by the fact that a conjugate heat transfer problem is solved, i.e. the equation describing the conservation of

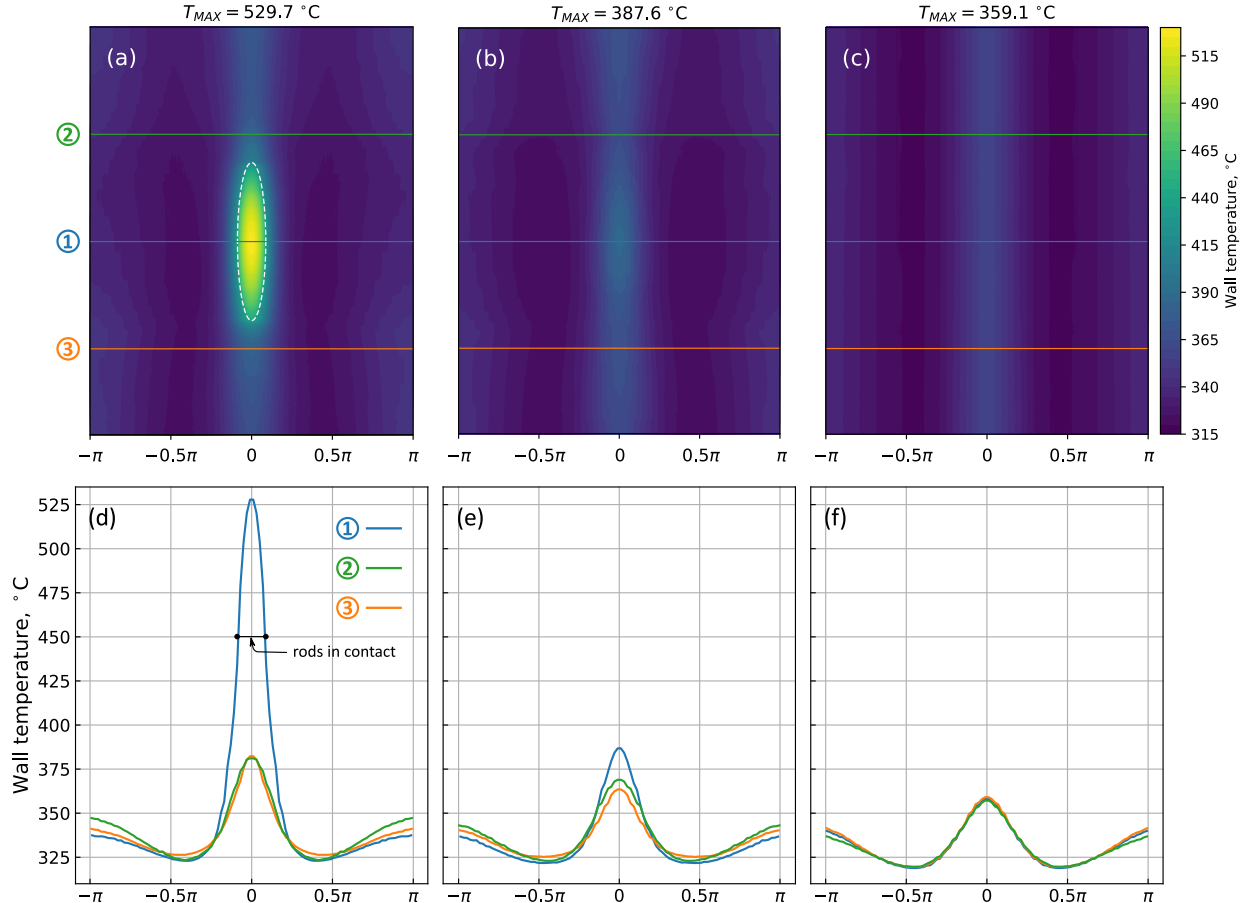


Figure 18: (a) – (c): wall temperature at the rod outer surface. (a): the case with rod and thimble in contact; (b): the case with 15% of the nominal gap distance between rod and thimble; (c): the nominal gap distance, non-deformed case. Flow direction in all figures from bottom to top. (d) – (f): respective wall temperature distributions along lines 1, 2 and 3.

energy is solved simultaneously inside the solid structure and in the coolant without imposing any specific heat transfer coefficient at the wet rod surface as in [23] but it is part of the coupled solution. The finite-volume mesh contains 22 Mio polyhedral cells and wall boundary cells are guaranteed to have centroid distances from the wall such that  $y_+ < 1$ . The momentum, energy and mass conservation equations are solved using segregated algorithms. The large sparse matrices constructed during this process are inverted using iterative solvers, e.g. conjugate gradient, generalised minimum residual (GMRES) and algebraic multigrid (AMG). As boundary conditions a uniform heat flux of about  $762 \text{ kW/m}^2$  is applied in the inner surface of the rod while the outer surface of the thimble and the top and bottom rod surfaces are considered adiabatic. Periodic boundary conditions are applied on the lateral faces of the computational domain to simulate the presence of surrounding rods/thimbles and the inlet mass flux is equal to  $1.844\text{E}+03 \text{ kg}/(\text{m}^2\text{s})$  and pressure is fixed at the domain outlet. Finally, two different maximum deformations are taken into account: the first one

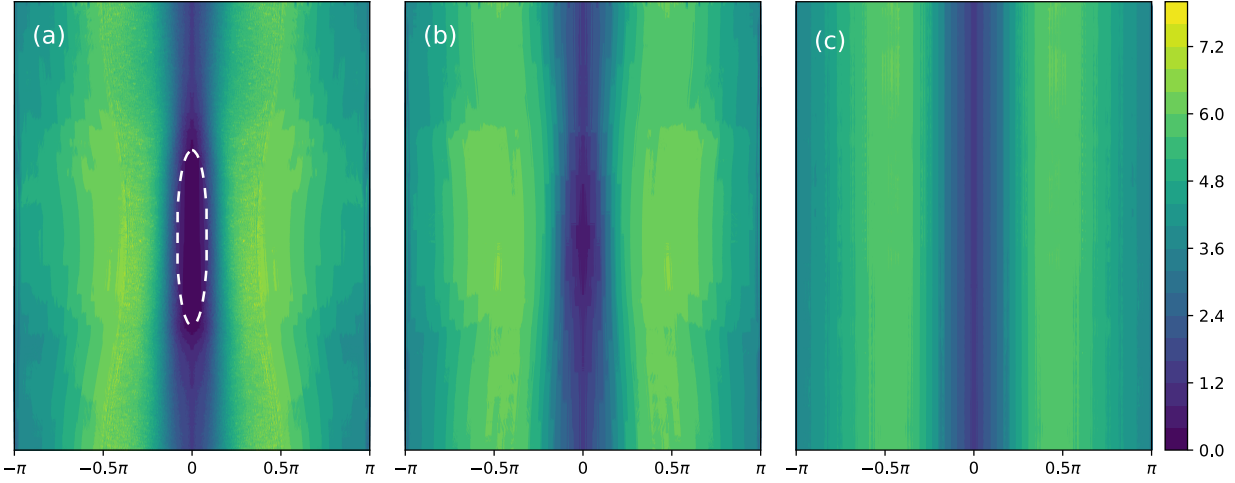


Figure 19: Wall shear stress magnitude. On the left the case with rod and thimble in contact; In the middle the case with 15% gap distance between rod and thimble; On the right the nominal, non-deformed case.

where the gap between the rod and thimble is only 15% of the nominal gap and the second one where the two solid structures are in contact with a contact area of 6.566229E-04 m<sup>2</sup> (representing 0.6% of the rod outer surface).

The results presented are in line with those of [23], however here the effect of neighboring heated structures is taken into account thanks to the fact that the complete conjugate heat transfer problem is solved and periodic boundary conditions are applied, introducing some azimuthal non-uniformity of the flow and consequently of the temperature field. Figure 18 depicts the rods surface temperatures for the cases with the solid structures in contact, with 15% gap distance and with nominal gap distance. It is possible to notice that because of the periodic lateral boundary conditions an azimuthal distribution of temperatures is present in all cases and it is strongly related to the wall distance between the neighboring surfaces and the resulting shear stress at the wall given by the local velocity profile as depicted in Figure 18: the closer are the neighboring surfaces the higher is the temperature at that particular azimuthal position. On the other hand at the azimuthal position where a maximum in the wall distance occurs, we see a minimum in the surface temperature. The opposite is true for the wall shear stress. The peak of temperature recorded in the nominal case is about 359°C, and it increases when the gap between the rod and the thimble is reduced to 15%, reaching almost 388°C at the position of minimum distance. In sub-cooled boiling, this jump in the surface temperature can decrease the local minimum DNBR of the system even if the average quantities are not so largely affected. When the two solid structures come to contact, a clear hot spot (almost 530°C) is recorded inside the contact area (delimited by the white dashed line in Figure 18). Even if these temperatures are far from the thermal limit of 1200°C, it is possible to see that, thanks to the thermal conductivity of the solid material a gradual decrease in the temperature field is recorded from the inside of the contact area towards the wet surface. On the surface wet by the coolant, the maximum temperatures are around 420°C, almost 60°C higher than the nominal case. This high-temperature increase

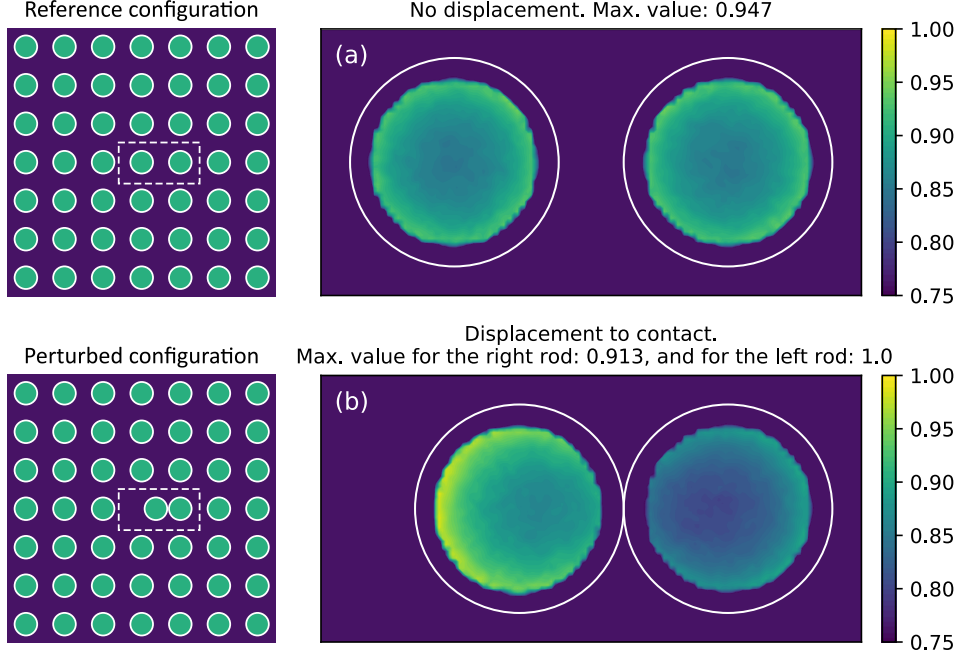


Figure 20: Internal rod power distribution in reference and bowed configuration. Fission powers are normalized to the maximum value in Figure (b) - Lower power values located at pins borders are caused by the use of a Cartesian mesh in the SERPENT tally specifications.

at the rods surface is caused by the fact that the coolant velocities close to the contact edge are very low and the convective transport is far from being optimal, and higher coolant temperatures are expected too in that position. In this type of extreme configurations, subchannel codes lack an appropriate way to model the contact and this significant increase in surface temperature from the nominal case is important if a more realistic prediction of the DNB is required. As stated before this simplified numerical model is only illustrative of the local effects present in single-phase flows and with the adiabatic wall for the thimble tube. From this type of analysis, it is clear that additional experimental data is auspicious for validating two-phase numerical models in deformed geometries as well.

#### 4.5. Neutronic effect on the internal rod power due to gap variation.

Since PWRs are under-moderated by design, from a neutronics perspective, the rod power increases when the gap increases (moderator addition) and conversely rod power reduces when the gap decreases (moderator removal). On the contrary, the outcome of previous sections is that when the gap increases, flow area between rods is increasing as well, and a more significant amount of coolant flows into the subchannel between the assemblies, see Figure 11. Consequently, it improves rod cooling, i.e., counteracting the effect of increased rod power. It affects all TH parameters as well as rod wall temperature and subsequently CHF; therefore, it reveals the importance of taking into account internal rod power moderation due to gap variation. Herein this power re-distribution due to change amount of coolant (moderator) will be referenced as a neutronic effect. In this section re-

sults of illustrative calculations of how internal rod power changes due to rod gap variation is presented, together with a qualitative comparison to the CFD results of a two-rod model.

The Monte Carlo based neutron transport code SERPENT [25] was used in this work for a qualitative evaluation of the pin power distribution inside a bowed pin. A simplified 2D representation of a PWR fuel assembly was modeled with SERPENT, neglecting the fuel assembly heterogeneities caused by guide tubes, different fuel enrichment or burnable poisons. The fuel assembly size was reduced to 1/4<sup>th</sup> because of symmetry reasons, but still providing enough surrounding environment for the neutron flux in target pins located in the center of the model. Two cases were developed: a reference case with fuel pins located at nominal configuration (i.e., constant pitch size) and a perturbed configuration, in which a fuel pin is displaced towards the right neighbor pin, letting the fuel clad touching. A sketch of the model is reported in Figure 20. Fuel temperature, coolant density, and coolant temperatures were set to constants values, representative of operational conditions. The model was loaded with fresh fuel (i.e. burnup = 0 MWd/KgHM). The use of a 2D model and a maximum fuel pin displacement was considered appropriate for a qualitative assessment of the bowing effect to the intra-pin power distribution because it represents a bounding case for more realistic 3D bowed configurations. The use of fresh fuel allows neglecting burnup effects that should be carefully evaluated at higher burnup because of rim effects. Actually, in the framework of burnup credit, a study about the effect of fuel pin bowing to the final material inventory has been conducted in [26]. In that study, a 3-dimensional 3×3 pin-cells lattice was modeled with the central pin bowed using a cosine profile (maximum displacement at the middle of axial elevation). The bowed pin was burned using an intra-pin fuel material discretization made of 4 radial layers, 8 azimuthal sectors and 40 axial segments, meaning that each segment was burned independently. In our model we do not consider burn-up effects, as well as 3-dimensional effects; however, the power inside the target fuel pin has been calculated using a higher mesh resolution of 20 radial layers and 16 azimuthal sectors.

The fission power was tallied in the bowed pin and its closest neighbor fuel pin using a regular Cartesian mesh with a bin size of ~0.3 mm in each dimension. Gamma smearing up-rate was not considered in these calculations. Concerning SERPENT options, neutron reflective spatial boundary conditions were employed and neutron population parameters were set to  $1 \times 10^9$  active histories, and  $5 \times 10^7$  discharged histories, ensuring the error of the calculated quantities to be below 0.2%. Concerning the nuclear data library, the JEFF3.2 [27] database was used. Results are reported in Figure 20, showing that in the bowed pin the power is tilted, with higher power regions located in the opposite direction of the bowing, because of the higher moderation experienced in that region. The relative difference in maximum power reaches a value of +5.4% compared to the reference case. However, it is clear that coupled neutronic, and fluid dynamics calculations are required in this case for more confident and quantitative answer on how neutronic effect may compensate the rod wall temperature.

## 5. Conclusions and Discussion

Results presented here show the assessment of subchannel code CTF on predicting the critical power in the  $4 \times 4$  tube bundle with rod bowing geometry. Based on the presented results, the following conclusions can be drawn:

- The main outcome of the subchannel method is that the rod bowing leads to a reduction of the critical power due to the reduction of the flow rate in a subchannel with reduced flow area, see Figure 11. W3 CHF correlation and Groeneveld CHF LUT reasonably predict DNBR except for the cases with rods in contact;
- For the reference test HTRF 166 with the straight rods, the Groeneveld CHF LUT yields a good agreement between calculated and measured critical powers and better agreement in comparison to W3 CHF correlation. The result of the mixing factor  $\beta$  variation showed that for  $\beta$  in the range of 0.09 – 0.15 the standard deviation of calculated critical power from the measured values is not changing (see Figure 4); therefore value 0.1 was chosen in all other HTRF tests;
- The spread of the critical power ratio values in the rod bowing to contact tests is quite high (see Figure 16) due to the local effects at the contact point, which cannot be captured by the subchannel method. The additional CFD calculations of two rods in contact showed a substantial rise in the wall temperature at the contact surface (see Figure 18(a) and (c)). The subchannel model, considered in this work, does not take into account the heat exchange between contacted rods. Due to the broad spread of critical power ratio distributions obtained for the tests HTRF 167 and HTRF 168 (see Figure 16), it can be concluded, that CHF models, in this case, require an additional function, which can take into account the substantial reduction of the critical power due to rods in contact;
- In this work, two configurations of partially rod bowing are considered: with 15% and 50% of the nominal gap between two rods correspondingly. For these configurations, the effect of partial rod bowing on the critical power is smaller than that of the rod bowing to contact. The reduction of the critical power caused by partially bowing rod does not require an additional correlated function since this reduction is successfully taken into account in the CHF models via mass flux variation. This is in line with [10, 13];
- As have been observed experimentally and in the presented results, the rod bow effect on the critical power strongly depends on thermal hydraulic parameters. For higher flow rates and pressure, CHF drops deeper more than for lower ones, see Figures 8 and 9;
- Neutronic calculations of the internal rod power have shown that reducing the gap between rods redistributes internal rod power as such that it reduces power at the rods contact point. It reduces the effect of over-heating at the rods contact point.

More sophisticated analytical tools than presently available are required to predict rod bowing with sufficient accuracy. Current functionality of CTF regarding modeling single-phase turbulent mixing is limited to either constant coefficient model or Rogers-Rosehart correlation, which is developed in the 70's last century. This approach requires revisiting with the application of modern findings in modeling turbulent flows with DNS and LES methods, which can be applied for the further development of the turbulent mixing in the subchannel approach. The CHF models used in present work have strong empirical relations with CHF test data, and it is difficult to compare the relative merits of these correlations due to lack of available information on the rod bowing tests. Measured critical power was obtained based on rods wall temperature at the five different elevations. Consequently, if CHF appeared in between the thermocouples, it will be detected once wall temperature excursion reaches one of the thermocouples. It imposes a drawback in obtaining critical power in HTRF tests which performed in the 70's last century and require to be repeated with modern experiment diagnostics and signal processing tools.

All CTF input decks used in this work are attached to the online version of this paper for further analysis and reproducibility of all results reported in this paper.

## 6. Acknowledgments

Within the STARS program at PSI (<http://www.psi.ch/stars>), research on development and validation of sub-channel and CFD methods for LWR core analyses is primarily conducted in the framework of collaboration with ENSI (H-101230). The assessment of these methods for bowed configurations presented here was performed through a complementary collaboration with Preussen Elektra.

## 7. Authors contribution

Roman Mukin derived the subchannel models and carried out the subchannel calculations. CFD analysis and MCNP neutronic calculations were performed by Riccardo Puragliesi and Marco Pecchia respectively. Roman Mukin prepared the manuscript with the input from all the authors.

## References

- [1] D. Reddy, C. Fighetti, Parametric study of CHF data, vol. 2: A generalized subchannel CHF correlation for PWR and BWR fuel assemblies. np-2609, Electric Power Research Institute, Palo Alto, CA.  
URL <https://www.epri.com/pages/product/NP-2609-V2/?lang=en>
- [2] D. Reddy, C. Fighetti, Parametric study of CHF data, vol. 3: Critical heat flux data. np-2609, Electric Power Research Institute, Palo Alto, CA.  
URL <http://www.epri.com/pages/product/NP-2609-V3P1/?lang=en>
- [3] R. J. Fetterman, F. Franceschini, Analysis of PWR assembly bow.
- [4] A. Heller, D. Farnsworth, E. McGuinn, Statistical methods applied to fuel rod bow analysis, Journal of Pressure Vessel Technology 109 (1) (1987) 147–152.
- [5] W. Ergen, Thermal bowing of fuel rods during transients, Journal of Nuclear Energy. Parts A/B. Reactor Science and Technology 18 (10) (1964) 537–545.

- [6] K. Hill, F. Motley, F. Cadek, J. Casterline, Effect of a rod bowed to contact on critical heat-flux in pressurized water-reactor rod bundles, in: Mechanical Engineering, Vol. 98, 1976, pp. 104–105.
- [7] K. Lund, ASME Paper No. 75-HT-49.
- [8] E. Markowski, L. Lee, R. Biderman, J. Casterline, Effect of rod bowing on CHF in PWR fuel assemblies, Am. Soc. Mech. Eng., [Pap.] (1977) 1–9.
- [9] Y. Nagino, N. Shodai, C. Matsumoto, M. Ueji, Rod bowed to contact departure from nucleate tests in coldwall thimble cell geometry, Journal of Nuclear Science and Technology 15 (8) (1978) 568–573.
- [10] Y. Nagino, N. Shodai, Chiehiro, M. M. Ito, M. Ueji, Effect of partially bowed heated rod on DNB in coldwall thimble cell geometry, Journal of Nuclear Science and Technology 15 (12) (1978) 943–945.
- [11] B. Pei, Y. Chen, C. Shih, W. Lin, Evaluations and modifications of the EPRI-1 correlation on PWR critical heat flux predictions under normal and abnormal fuel conditions, Nuclear Technology 75 (2) (1986) 134–147.
- [12] H.-J. Paik, S.-G. Yang, A new design procedure for the evaluation of rod bow DNBR penalty, Nuclear Engineering and Technology 28 (3) (1996) 331–338.
- [13] X. Zejun, S. Xianhui, L. Xuemei, B. Xuesong, M. Jieliang, W. Pengfei, C. Bingde, Experimental research progress on critical heat flux of Chinese PWR, Nuclear Engineering and Design 229 (2) (2004) 213 – 222. doi:<https://doi.org/10.1016/j.nucengdes.2003.12.005>.
- [14] L. Tong, Heat transfer in water-cooled nuclear reactors, Nuclear Engineering and Design 6 (4) (1967) 301–324.
- [15] L. Tong, Boiling crisis and critical heat flux., Tech. rep., Westinghouse Electric Corp., Pittsburgh, Pa. (1972).
- [16] L. Tong, Phenomenological study of critical heat-flux, in: Mechanical Engineering, Vol. 97, 1975, pp. 105–105.
- [17] D. Groeneveld, J. Shan, A. Vasić, L. Leung, A. Durmayaz, J. Yang, S. Cheng, A. Tanase, The 2006 CHF look-up table, Nuclear Engineering and Design 237 (15) (2007) 1909–1922.
- [18] M. Avramova, CTF - a thermal-hydraulic subchannel code for LWRs transient analyses. users manual, Tech. rep., Pennsylvania State University (June, 2014).
- [19] R. K. Salko, M. Avramova, CTF theory manual.
- [20] R. K. Salko, M. Avramova, COBRA-TF Subchannel Thermal-Hydraulics Code (CTF). Theory Manual, Revision 0, Tech. rep. (March, 2015).
- [21] R. Salko, T. Blyth, C. Dances, J. Magedanz, M. Avramova, S. Palmtag, J. Gehin, CTF validation, Tech. rep. (2014).
- [22] J. Rogers, R. Rosehart, Mixing by turbulent interchange in fuel bundles. correlations and influences, in: ASME, 1972, pp. 1–12, paper 75-HT-31.
- [23] I. Nakajima, A. Kikuchi, T. Kobori, A study of the effect of rod-bowing on critical heat flux, Nuclear Engineering and Design 42 (2) (1977) 237 – 245.
- [24] A. Rubin, A. Schoedel, M. Avramova, H. Utsuno, S. Bajorek, A. Velazquez-Lozada, OECD/NRC benchmark based on NUPEC PWR subchannel and bundle tests (PSBT), volume i: Experimental database and final problem specifications, US NRC OECD Nuclear Energy Agency.
- [25] J. Leppänen, M. Pusa, T. Viitanen, V. Valtavirta, T. Kaltiaisenaho, The serpent monte carlo code: Status, development and applications in 2013, Annals of Nuclear Energy 82 (2015) 142–150.
- [26] J. Li, D. Rochman, J. Herrero, A. Vasiliev, H. Ferroukhi, A. Pautz, M. Seidl, D. Janin, UO<sub>2</sub> fuel pin bowing effects on isotopic concentrations, Annals of Nuclear Energy 105 (2017) 361 – 368.
- [27] A. Koning, E. Bauge, C. Dean, E. Dupont, U. Fischer, R. Forrest, R. Jacqmin, H. Leeb, M. Kellett, R. Mills, et al., Status of the JEFF nuclear data library, J. Korean Phys. Soc 59 (2) (2011) 1057–1062.

## Appendix A. Filtering of HTRF tests data

Complete HTRF database used in this work is presented in Table A.2. Through the calculations with the boundary conditions and the critical power measured in ther tests, it is found that for some tests CHF is located beyond the range, where thermocouples

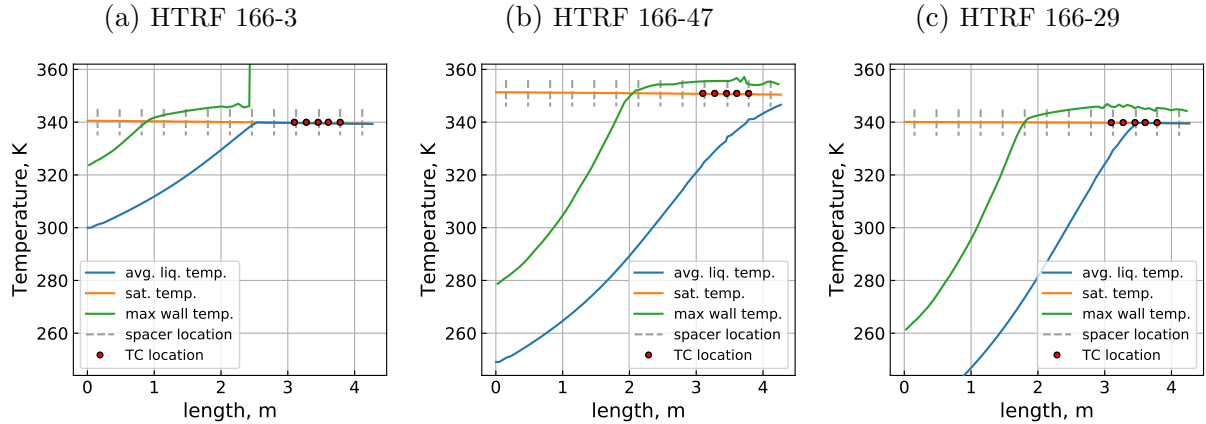


Figure A.21: Examples of average liquid, saturation and maximum wall temperatures distributions for two tests which are filtered (a) and (b) due to location of CHF is before and after the thermocouples (TC) positions respectively; (c) an example of temperatures distributions for the selected test.

were placed. CHF occurs downstream of the location of onset of nucleate boiling (when wall temperature above saturation temperature) and before the location where the water is completely evaporated (rapid wall temperature rising). Thus if the calculated rapid wall temperature rise is located before the thermocouples window, or liquid temperature remain below the liquid saturation temperature then the data point is considered to be unreasonable and is filtered out from the further consideration. An examples of such cases are presented in Figure A.21. Also those cases have been selected for which both CHF models give converged solution.

Table A.2: HTRF tests main parameters, taken from [2] pp. 763 – 792.

Test name	Pressure, bar	Temperature, °C	Flow rate, kg/s	Power, MW		
				Measured	Groeneveld	W3
HTRF 166-1	103.4	296.4	8.7889	2.8286	-	-
HTRF 166-2	124.1	290.0	8.9013	2.9918	2.94502	3.04019
HTRF 166-3	144.8	299.9	6.3963	3.2365	-	-
HTRF 166-4	165.8	298.0	9.0979	3.7601	-	-
HTRF 166-5	165.8	294.5	7.6245	2.6246	-	-
HTRF 166-6	144.9	297.4	7.5326	3.0258	2.85454	2.75433
HTRF 166-7	144.8	294.6	6.3197	2.5838	2.52543	2.52239
HTRF 166-8	165.5	291.3	6.3070	2.9714	2.95406	2.8265
HTRF 166-9	165.5	295.0	5.1962	2.5226	2.45076	2.3668
HTRF 166-10	165.8	312.5	7.6526	2.7878	-	-
HTRF 166-11	144.8	317.4	7.5173	2.3730	-	-
HTRF 166-12	144.8	313.7	9.0162	2.8830	-	-
HTRF 166-13	165.5	319.2	8.9013	2.8626	-	-
HTRF 166-14	165.5	269.7	5.1477	2.9170	-	-
HTRF 166-15	144.8	273.8	5.1681	2.7606	2.60214	2.6529

continued ...

Test name	Pressure, bar	Temperature, °C	Flow rate, kg/s	Power, MW		
				Measured	Groeneveld	W3
HTRF 166-16	144.4	270.8	6.4959	3.3725	3.19436	3.18933
HTRF 166-17	166.2	276.0	6.3785	3.2569	3.38231	3.26583
HTRF 166-18	124.5	295.7	8.8323	3.0326	-	-
HTRF 166-19	124.1	268.4	5.0890	2.5158	2.45341	2.61972
HTRF 166-20	103.4	268.1	6.3785	2.8422	2.64639	2.85771
HTRF 166-21	103.4	273.1	8.8885	3.3521	-	-
HTRF 166-22	103.4	245.4	5.2626	2.8354	-	-
HTRF 166-23	124.5	247.9	5.1860	2.9510	2.83114	3.02099
HTRF 166-24	144.8	245.4	3.9425	2.6178	2.90063	3.04212
HTRF 166-25	144.8	251.8	5.1528	3.1413	2.55048	2.65739
HTRF 166-26	165.8	253.3	5.1018	3.2433	3.03529	3.09427
HTRF 166-27	165.8	242.5	3.7867	2.7538	-	-
HTRF 166-28	165.8	228.6	3.8582	2.9102	-	-
HTRF 166-29	145.1	224.9	3.7842	2.9034	2.76607	2.88469
HTRF 166-30	145.8	222.5	5.1426	3.6717	3.64009	3.6839
HTRF 166-31	124.1	226.6	5.0839	3.3045	3.27247	3.41298
HTRF 166-32	103.8	221.7	5.0966	3.1277	3.22081	3.40788
HTRF 166-33	103.8	222.2	5.0941	3.1345	3.21511	3.39617
HTRF 166-34	103.4	205.4	3.8429	2.8558	2.94912	3.12124
HTRF 166-35	103.8	222.8	3.8301	2.6926	2.70769	2.8855
HTRF 166-36	145.5	206.2	3.8148	3.0394	3.06175	3.17831
HTRF 166-37	165.1	207.1	3.8097	3.1685	-	-
HTRF 166-38	165.8	288.9	7.6782	3.5493	-	-
HTRF 166-39	165.5	269.9	7.6756	4.1137	-	-
HTRF 166-40	144.8	272.5	7.6526	3.6377	3.6354	3.54454
HTRF 166-41	124.5	268.8	8.9319	3.8553	3.73241	3.78121
HTRF 166-42	103.8	252.9	6.3555	3.0665	-	-
HTRF 166-43	145.1	248.7	6.3963	3.5697	3.7336	3.71822
HTRF 166-44	166.2	249.1	6.4219	3.6105	3.61074	3.59655
HTRF 166-45	144.8	252.7	6.3631	3.6649	3.56174	3.73808
HTRF 166-46	103.4	205.4	5.1681	3.5017	3.89409	3.92537
HTRF 166-47	144.8	210.1	5.1477	3.5697	-	-
HTRF 167-1	103.4	291.6	9.1796	3.0597	-	-
HTRF 167-2	124.1	293.8	8.9881	3.0054	2.72582	2.67921
HTRF 167-3	144.4	291.6	9.0238	2.9714	3.22097	3.09167
HTRF 167-4	165.1	294.0	9.1413	2.8286	3.54916	3.41822
HTRF 167-5	165.5	291.4	5.1784	2.0738	2.42501	2.31039
HTRF 167-6	165.5	288.0	6.5240	2.3730	2.93688	2.81838
HTRF 167-7	144.8	297.6	6.3606	2.4682	2.37557	2.27299
HTRF 167-8	144.8	292.8	7.7216	2.8422	2.84801	2.73317
HTRF 167-9	165.5	291.0	7.7343	2.6926	3.22042	3.1064
HTRF 167-10	165.5	313.4	7.6705	2.3322	2.56673	2.37621
HTRF 167-11	145.1	316.1	7.6654	2.4274	2.1781	2.01159

continued ...

Test name	Pressure, bar	Temperature, °C	Flow rate, kg/s	Power, MW		
				Measured	Groeneveld	W3
HTRF 167-12	144.8	317.0	8.8885	2.6450	2.36203	2.16876
HTRF 167-13	165.5	314.6	8.9396	2.5090	2.82834	2.60767
HTRF 167-14	165.5	270.5	5.2090	2.2982	2.84727	2.76862
HTRF 167-15	145.1	277.7	5.0686	2.4002	2.44364	2.38065
HTRF 167-16	144.8	270.9	6.4908	2.7674	3.06384	2.96673
HTRF 167-17	165.5	272.8	6.4602	2.6110	3.27508	3.1943
HTRF 167-18	144.8	274.3	7.6858	2.9850	3.33124	3.26567
HTRF 167-19	124.8	271.1	5.0609	2.5294	2.38771	2.35519
HTRF 167-20	103.8	274.7	6.2840	2.8082	-	-
HTRF 167-21	103.4	268.2	8.9779	3.5153	3.52233	3.47558
HTRF 167-22	124.1	269.3	8.9676	3.6241	2.79191	2.73051
HTRF 167-23	125.1	252.1	5.1094	2.6994	2.77853	2.73769
HTRF 167-24	104.5	245.1	5.1707	2.9578	2.85454	2.84968
HTRF 167-25	103.4	256.5	6.4040	3.0801	2.63303	2.61492
HTRF 167-26	144.8	238.4	3.9042	2.3458	-	-
HTRF 167-27	165.5	248.9	3.8761	2.1622	-	-
HTRF 167-28	165.5	248.2	5.1401	2.5566	-	-
HTRF 167-29	144.8	248.7	5.1145	2.5430	3.02089	2.96731
HTRF 167-30	144.8	224.8	3.8633	2.3458	2.81244	2.79981
HTRF 167-31	165.5	228.1	3.8608	2.3118	-	-
HTRF 167-32	165.5	225.8	5.1349	2.7742	-	-
HTRF 167-33	144.8	225.8	5.1069	2.8014	3.43641	3.40784
HTRF 167-34	124.5	226.6	5.0915	2.8762	3.27508	3.19802
HTRF 167-35	107.9	236.7	5.0175	2.9714	2.92606	2.85748
HTRF 168-1	103.4	297.9	8.8119	2.8014	-	-
HTRF 168-2	124.1	295.5	8.8859	3.1413	2.72287	2.68749
HTRF 168-3	147.2	294.1	8.8987	2.9034	3.25224	3.11176
HTRF 168-4	164.8	296.9	9.2179	2.8286	3.56447	3.42105
HTRF 168-5	165.8	295.1	5.1835	2.0602	2.40125	2.29216
HTRF 168-6	165.5	293.8	6.4040	2.3526	2.81905	2.69322
HTRF 168-7	144.8	297.7	6.2891	2.5430	2.4086	2.3219
HTRF 168-8	144.8	293.1	6.3708	2.6586	2.54184	2.45999
HTRF 168-9	145.1	297.3	7.5684	2.8422	2.75833	2.6402
HTRF 168-10	165.5	295.4	7.7726	2.6790	3.19668	3.06211
HTRF 168-11	165.8	314.5	7.7190	2.3526	2.61131	2.42006
HTRF 168-12	145.1	312.9	7.7165	2.4886	2.33966	2.18145
HTRF 168-13	144.8	317.4	8.8298	2.6246	-	-
HTRF 168-14	165.5	317.3	8.9217	2.5158	2.79939	2.57488
HTRF 168-15	165.5	272.6	5.1554	2.2982	-	-
HTRF 168-16	144.8	271.1	5.1554	2.5566	2.64435	2.6071
HTRF 168-17	145.1	271.1	6.4934	2.8082	3.14817	3.06491
HTRF 168-18	165.5	274.1	6.4474	2.6382	3.31995	3.23905
HTRF 168-19	144.8	272.3	7.6296	3.0190	3.46104	3.40432

continued ...

Test name	Pressure,	Temperature,	Flow rate,	Power, MW		
	bar	°C	kg/s	Measured	Groeneveld	W3
HTRF 168-20	123.8	271.4	5.1426	2.5226	2.41106	2.43683
HTRF 168-21	103.8	272.4	6.3785	2.8694	-	-
HTRF 168-22	123.8	248.3	5.1605	2.8966	2.87893	2.8919
HTRF 168-23	103.4	245.6	5.1145	2.8694	-	-
HTRF 168-24	103.1	248.1	6.4704	3.3249	3.12239	3.1381
HTRF 168-25	144.8	252.4	3.8276	2.3254	2.39074	2.43077
HTRF 168-26	165.1	252.5	3.8250	2.1350	-	-
HTRF 168-27	165.1	248.8	5.1962	2.5090	-	-
HTRF 168-28	145.1	247.0	5.1809	2.6994	3.153	3.10503
HTRF 168-29	145.5	227.1	3.7638	2.4546	2.72309	2.78844
HTRF 168-30	165.5	224.2	3.7918	2.2778	-	-
HTRF 168-31	165.1	229.6	5.1988	2.6858	-	-
HTRF 168-32	144.8	229.0	5.2013	2.8694	-	-
HTRF 168-33	124.1	228.1	5.1401	3.1345	3.27432	3.27376
HTRF 168-34	103.4	224.9	5.1222	3.1277	3.17518	3.1652
HTRF 168-35	103.1	220.2	3.7893	2.5906	-	-
HTRF 168-36	103.4	205.6	3.8429	2.8082	2.94976	2.94363
HTRF 168-37	166.2	202.1	3.8301	2.4886	-	-
HTRF 168-38	144.8	207.5	3.8046	2.6790	-	-
HTRF 168-39	104.5	275.2	8.8578	3.5221	-	-
HTRF 168-40	103.4	272.4	8.9242	3.5289	-	-
HTRF 168-41	124.1	272.6	8.9319	3.6445	3.50376	3.45929
HTRF 168-42	144.8	268.2	5.1681	2.7402	2.70986	2.66717
HTRF 168-43	165.8	252.7	6.0823	2.9850	-	-
HTRF 168-44	144.8	254.1	6.3376	3.0190	3.45649	3.42124
HTRF 168-45	144.8	204.0	3.7586	2.7130	-	-
HTRF 168-46	144.8	299.4	6.2763	2.6246	-	-
HTRF 168-47	165.5	295.9	6.4883	2.4546	2.78731	2.66147
HTRF 168-48	166.2	296.1	5.0762	2.1758	2.34459	2.24205
HTRF 168-49	165.8	296.8	7.7599	2.7130	3.15195	3.01699
HTRF 168-50	145.8	299.4	7.5837	2.8898	-	-
HTRF 168-51	165.8	268.3	5.2345	2.4954	-	-
HTRF 168-52	145.1	273.8	5.0915	2.6994	2.57296	2.53131
HTRF 168-53	144.4	270.3	6.5930	3.0462	3.18927	3.11076
HTRF 168-54	165.5	268.5	6.5317	2.8082	3.48564	3.41697
HTRF 168-55	145.1	244.2	3.8250	2.5566	2.51163	2.55938
HTRF 168-56	165.8	244.0	3.7816	2.2914	-	-
HTRF 168-57	165.5	246.8	5.2039	2.6654	-	-
HTRF 168-58	145.1	251.7	5.1324	2.8422	3.03981	3.00022
HTRF 168-59	144.8	249.6	6.5393	3.1277	3.63102	3.62422
HTRF 168-60	165.1	247.4	6.4832	3.0122	-	-
HTRF 168-61	145.1	225.0	3.6540	2.6518	2.6878	2.7634
HTRF 168-62	165.1	216.4	3.9374	2.4954	-	-

continued ...

Test name	Pressure,	Temperature,	Flow rate,	Power, MW		
	bar	°C	kg/s	Measured	Groeneveld	W3
HTRF 168-63	165.5	225.9	5.1349	2.8150	-	-
HTRF 168-64	144.8	225.6	5.1401	2.9850	3.52297	3.51679
HTRF 168-65	165.1	204.8	3.8710	2.5294	-	-
HTRF 169-1	103.8	295.8	8.8400	2.9782	-	-
HTRF 169-2	123.8	295.4	8.8374	3.0258	-	-
HTRF 169-3	144.4	297.4	8.9064	3.1889	3.1166	2.9793
HTRF 169-4	165.8	300.4	8.9396	3.7193	-	-
HTRF 169-5	145.1	299.1	8.9013	3.3249	-	-
HTRF 169-6	165.5	292.3	5.6329	2.4886	2.6408	2.5238
HTRF 169-7	165.8	295.3	6.3963	2.8150	-	-
HTRF 169-8	145.8	293.7	6.3683	2.5906	2.5707	2.4810
HTRF 169-9	145.1	293.8	7.6220	2.9850	2.8970	2.7990
HTRF 169-10	166.2	294.9	7.6348	3.3113	-	-
HTRF 169-11	166.9	315.2	7.4637	2.7266	-	-
HTRF 169-12	144.8	319.8	7.6245	2.2506	2.1624	1.9646
HTRF 169-13	144.8	311.3	8.9574	2.8082	-	-
HTRF 169-14	165.5	320.7	8.8170	2.8830	-	-
HTRF 169-15	165.1	266.9	5.1554	2.7538	-	-
HTRF 169-16	145.8	275.8	5.1018	2.5498	2.5426	2.5282
HTRF 169-17	144.8	269.9	6.3555	3.1685	3.1615	3.0725
HTRF 169-18	168.6	273.4	6.4193	3.2705	-	-
HTRF 169-19	145.8	270.0	7.6526	3.4949	3.5846	3.5353
HTRF 169-20	124.5	271.1	5.0328	2.4274	2.3901	2.4440
HTRF 169-21	103.4	270.8	6.3478	2.8694	2.5745	2.6511
HTRF 169-22	103.4	268.8	8.9549	3.6377	3.2098	3.2975
HTRF 169-23	124.5	248.0	5.1043	2.8694	2.8709	2.9177
HTRF 169-24	104.5	248.2	5.1120	2.7878	2.7410	2.7852
HTRF 169-25	103.4	248.1	6.3657	3.2229	3.1016	3.1593
HTRF 169-26	145.1	248.6	3.7408	2.4614	2.4064	2.4798
HTRF 169-27	165.8	245.8	3.8250	2.5090	-	-
HTRF 169-28	165.5	245.3	5.1298	3.0733	-	-
HTRF 169-29	145.1	242.1	5.1273	3.0529	3.2234	3.2274
HTRF 169-30	144.8	226.6	3.8863	2.8014	2.7917	2.8844
HTRF 169-31	165.1	230.3	3.8301	2.6178	-	-
HTRF 169-32	165.5	227.7	5.2192	3.5221	-	-
HTRF 169-33	145.1	229.9	5.2141	3.1345	3.5121	3.5144
HTRF 169-34	165.8	227.2	5.1528	3.3045	-	-
HTRF 169-35	124.8	221.0	5.1349	3.2229	3.4168	3.4541
HTRF 169-36	103.1	219.4	5.1503	3.1345	3.2736	3.3092
HTRF 169-37	103.8	222.4	6.4474	3.5969	3.7498	3.7794
HTRF 169-38	103.4	227.4	3.8250	2.5090	2.6380	2.6887
HTRF 169-39	103.4	200.7	3.8736	2.8898	3.0348	3.0684
HTRF 169-40	145.8	203.1	3.8225	3.0394	3.1116	3.2222

continued ...

Test name	Pressure, bar	Temperature, °C	Flow rate, kg/s	Power, MW		
				Measured	Groeneveld	W3
HTRF 169-41	165.1	201.6	3.8710	3.0122	-	-
HTRF 169-42	124.5	226.8	3.7689	2.6110	2.6374	2.7173
HTRF 169-43	103.1	223.1	3.8276	2.5702	2.7030	2.7543
HTRF 169-44	125.1	227.6	5.1349	3.2433	3.2854	3.3276
HTRF 169-45	144.4	250.7	3.7638	2.4410	-	-
HTRF 169-46	124.5	267.7	8.9293	3.7737	3.6991	3.6753
HTRF 169-47	145.1	252.7	6.2814	3.4745	3.5106	3.4910
HTRF 169-48	165.5	246.8	6.4040	3.7805	-	-
HTRF 170-1	103.4	295.0	8.8834	2.9646	-	-
HTRF 170-2	124.5	290.1	9.0928	3.1685	3.00746	3.05256
HTRF 170-3	145.1	297.2	8.8093	3.3725	-	-
HTRF 170-4	166.5	292.8	5.1094	2.4478	-	-
HTRF 170-5	165.1	293.8	6.3529	2.8558	-	-
HTRF 170-6	144.8	296.2	6.3248	2.6110	2.49053	2.46845
HTRF 170-7	145.8	292.9	7.6731	3.0462	-	-
HTRF 170-8	165.8	295.7	7.6143	3.2637	-	-
HTRF 170-9	165.5	315.4	7.6373	2.2778	2.67522	2.46931
HTRF 170-10	145.1	316.4	7.6143	2.5022	-	-
HTRF 170-11	144.4	320.2	8.8093	2.6382	-	-
HTRF 170-12	165.5	319.9	8.8681	2.8830	-	-
HTRF 170-13	164.4	275.9	5.1988	2.6790	2.84086	2.77322
HTRF 170-14	145.1	271.5	5.0813	2.5362	2.61003	2.67144
HTRF 170-15	144.8	272.1	6.3963	3.0190	3.12749	3.11812
HTRF 170-16	165.8	274.9	6.4832	3.2161	3.40993	3.32846
HTRF 170-17	145.1	271.2	7.6348	3.5493	3.618	3.57059
HTRF 170-18	125.1	257.3	5.0813	2.3934	-	-
HTRF 170-19	104.1	271.4	6.3274	2.6518	2.56087	2.72611
HTRF 170-20	104.5	276.3	8.8374	3.3249	-	-
HTRF 170-21	124.5	248.2	5.2652	2.7538	2.92637	3.05867
HTRF 170-22	103.4	251.2	5.0252	2.5158	2.67149	2.8033
HTRF 170-23	104.5	247.7	6.3759	3.0462	3.11166	3.27478
HTRF 170-24	165.5	246.4	3.8684	2.4274	-	-
HTRF 170-25	167.9	250.2	3.8199	2.5022	-	-
HTRF 170-26	165.5	252.1	5.1452	3.0394	-	-
HTRF 170-27	145.8	252.9	5.0609	2.9442	2.98907	3.04634
HTRF 170-28	145.1	298.1	6.3197	2.5974	-	-
HTRF 170-29	145.8	228.2	3.8608	2.7130	-	-
HTRF 170-30	165.8	232.5	3.8327	2.7402	-	-
HTRF 170-31	165.5	228.1	7.2620	3.5017	-	-
HTRF 170-32	145.8	227.7	5.1809	3.2773	3.54956	3.60284
HTRF 170-33	125.1	231.3	5.0660	3.0529	3.18003	3.30798
HTRF 170-34	103.1	226.7	5.0762	2.8694	3.12185	3.24191
HTRF 170-35	103.8	274.9	6.2814	2.6246	2.46983	2.64691

continued ...

Test name	Pressure, bar	Temperature, °C	Flow rate, kg/s	Power, MW		
				Measured	Groeneveld	W3
HTRF 170-36	104.5	273.1	8.9064	3.3453	-	-
HTRF 170-37	104.5	247.3	5.0558	2.5838	2.73974	2.87431
HTRF 170-38	103.1	251.8	6.4500	3.0190	3.02428	3.18922
HTRF 170-39	103.1	225.2	6.4091	3.4405	3.64999	3.79557
HTRF 170-40	103.4	230.1	3.8480	2.3866	2.61268	2.73417
HTRF 170-41	103.8	199.1	4.2259	2.7470	-	-
HTRF 170-42	104.5	209.0	5.0558	3.1617	3.44907	3.56984
HTRF 170-43	145.5	205.2	3.9119	2.9646	3.13716	3.25647
HTRF 170-44	161.3	204.4	3.9170	3.0665	-	-
HTRF 170-45	165.5	226.8	5.1401	3.4609	-	-
HTRF 170-46	145.1	250.0	6.3734	3.4677	3.68697	3.67647
HTRF 170-47	124.5	270.7	8.9728	3.5153	3.66441	3.68468
HTRF 170-48	165.1	301.8	8.2961	3.5629	-	-